Machine Learning Assisted Chemical Characterization and Optical Properties of Atmospheric Brown Carbon in Nanjing, China

Yu Huang[1], Xingru Li[2], Dan Dan Huang[3], Ruoyuan Lei[1], Binhuang Zhou[1], Yunjiang Zhang[1], Xinlei Ge[1, 4*]

[1] Jiangsu Key Laboratory of Atmospheric Environment Monitoring and Pollution Control, Collaborative Innovation Center of Atmospheric Environment and Equipment Technology, School of Environmental Science and Engineering, Nanjing University of Information Science and Technology, Nanjing 210044, China

[2] Analytical Instrumentation Center, Department of Chemistry, Capital Normal University, Beijing, 100048, China

[3] Shanghai Academy of Environmental Sciences, Shanghai 200233, China

[4] School of Environment and Energy Engineering, Anhui Jianzhu University, Hefei 230601, China

*Corresponding author: Xinlei Ge (Email: caxinra@163.com)

For *Atmospheric Chemistry and Physics*

Abstract: The light-absorbing organics, namely brown carbon (BrC), can significantly affect atmospheric visibility and radiative forcing, yet current knowledge of chemical composition of BrC is largely limited to a number of certain classes of compounds; the chemical and optical properties, and particularly linkage between the two remain poorly understood. To address this, a comprehensive analysis was conducted on the particulate matter ($PM_{2.5}$) samples collected in Nanjing, China during 2022 ~ 2023 with a focus on the identification of key BrC molecules. Several important clues related to BrC were found. First, the water-soluble organic aerosol (WSOA) was more oxygenated during cold season (CS) due to a highly oxidized secondary OA (SOA) factor that was strongly associated with aqueous/heterogeneous reactions especially during nighttime, while the WSOA during summer season (SS) was less oxygenated and the SOA was mainly from photochemical reactions. Fossil fuel combustion hydrocarbon-like OA was the largest and dominant contributor to the light absorption during CS (55.6 ~ 63.7%). Secondly, our observations reveals that aqueous oxidation can lead to notable photo-enhancement during CS, while photochemical oxidation on the contrary caused photo-bleaching during SS; Both water-soluble and methanol-soluble organics had four key fluorophores, including three factors relevant with humic-like substances (HULIS) and one protein-like component. Thirdly, molecular characterization show that CHON compounds were overall the most abundant species, followed by CHO and CHN compounds, and significant presence of organosulfates in CS samples reaffirmed the importance of aqueous-phase formation. Finally, building upon the molecular characterization and light absorption measurement results, the machine learning approach was applied to identify the key BrC molecules, and 31 compounds including polycyclic aromatic hydrocarbons (PAHs), oxyheterocyclic PAHs, quinones, and nitrogen-containing species, etc., which can be a good reference for future studies.

1 Introduction

In ambient air, some organic aerosol (OA) species can absorb light in the near-ultraviolet (UV) and visible spectrum, termed as "brown carbon (BrC)" (Andreae and Gelencsér, 2006; Chen et al., 2020b). The BrC absorption exhibits strong wavelength-dependence that typically the absorption increases as the wavelength decreases (Laskin et al., 2015); it can also contribute to the darkening of ice and snow surfaces, particularly in low-latitude and polar regions (Yan et al., 2018; Brown et al., 2022; Chakrabarty et al., 2023). Thus, BrC can play a crucial role in global climate and air quality (Jo et al., 2016; Feng et al., 2013). Some studies show that the global radiative forcing of BrC ranges from approximately 0.22 to 0.57 W m^{-2}, equivalent to 27 ~ 70 % of that of black carbon (BC) (Lin et al., 2014; Zhang et al., 2017). Xu et al. (2024) used a global climate model to estimate that BrC accounts for 19% and 12% of the total light absorption by carbonaceous aerosols, with the direct radiative forcing of 0.110 W m^{-2} and 0.205 W m^{-2} in China during winter and summer, respectively. Delessio et al. (2024) estimated a top-of-the-atmosphere (TOA) radiative effect of BrC to be 0.04 W m^{-2}.

The sources of atmospheric BrC are highly complex, as it can originate from multiple primary sources (Hecobian et al., 2010; Chakrabarty et al., 2010; Gu et al., 2022) as well as various secondary chemical processes (Wang et al., 2021) (Fleming et al., 2020; Jiang et al., 2021; Chen et al., 2020b). The primary sources mainly include coal combustion, biomass burning, and vehicular emissions (Wang et al., 2016; Sun et al., 2016; Qi et al., 2019; Chen et al., 2018; Gu et al., 2022); besides, a significant presence of chromophores originating from the ocean has been observed, indicating that the ocean/marine emission is likely also an important source of BrC (Cavalli et al., 2004). As said, secondary BrC species can be generated from many processes, for instances, the aromatic secondary OA (SOA) species formed under high NO$_x$ concentrations (Jaoui et al., 2006), reaction products of biogenic or anthropogenic SOAs with nitrogen-containing substances such as NH$_3$ and NH$_4^+$ (Updyke et al., 2012; Shapiro et al., 2009; Bones et al., 2010), and aqueous-phase reaction products from various carbonyl/phenolic precursors in cloud, fog, and aerosol water (Hu et al., 2017;

74   Wang et al., 2021; Li et al., 2023; Ou et al., 2021).

75   The optical properties of BrC are closely related with sources and composition of

76   OA. Recent studies have linked BrC light absorption with various sources resolved

77   from factor analysis of OA determined by the aerosol mass spectrometry (AMS) (Chen

78   et al., 2020b; Zhong et al., 2023; Chen et al., 2016), and provided the mass absorption

79   efficiency (MAE) of individual BrC source/factor. Current studies have identified

80   several classes of light-absorbing organics in ambient OA, such as aromatic carboxylic

81   acids, phenols, nitroaromatic compounds (NACs), polycyclic aromatic hydrocarbons

82   (PAHs) and their derivatives (Lin et al., 2018; Huang et al., 2018; Wang et al., 2021;

83   Xing et al., 2023; Gu et al., 2022; Chen et al., 2020b; Kuang et al., 2023; Laskin et al.,

84   2025). Some lignin pyrolysis/burning products including coumarins, flavonoids,

85   stilbenes, and several sulfur-containing species are also significant BrC constituents

86   (Fleming et al., 2020; Budisulistiorini et al., 2017; Huang et al., 2022). Xing et al. (2023)

87   identified a series of BrC chromophores, encompassing nitrophenols, benzoic acids,

88   oxygenated PAHs, phenols, aryl amides/amines, phenylpropene derivatives, coumarins

89   and flavonoids, pyridines, and nitrobenzoic acids. Nevertheless, knowledge regarding

90   the molecular composition of BrC so far is still incomplete and the identified species

91   only occupy a limited fraction of the BrC total light absorption (<25%) (Wang et al.,

92   2024). For examples, Zhang et al. (2013) measured eight NACs in Los Angeles and

93   found that they contributed about 4 % of water-soluble BrC light absorption at 365 nm;

94   Huang et al. (2018) measured 18 PAHs and their derivatives in Xi'an and found that

95   they accounted for on average ∼ 1.7 % of the overall absorption of methanol-soluble

96   BrC; Gu et al. (2022) quantified eight NACs present in $PM_{2.5}$ during winter in Nanjing,

97   which together accounted for at most ∼9 % of the total BrC absorption at 365 nm. On

98   the other hand, the fluorescent properties of OA can be determined by the excitation-

99   emission matrix (EEM) fluorescence spectroscopy (Murphy et al., 2013; Stubbins et al.,

100   2014). By performing the parallel factor analysis (PARAFAC) on EEM data, the key

101   fluorophores can be identified (Xie et al., 2020; Chen et al., 2020a; Chen et al., 2021).

102   These fluorophores are also linked with different sources such as biomass burning, coal

103   combustion, and vehicle emissions (Tang et al., 2020).

104   Emerging non-targeted approaches based on gas chromatography (GC) or liquid

105   chromatography (LC) coupled with high-resolution mass spectrometry can detect

106   hundreds to thousands of molecules in OA (Kuang et al., 2023; Mao et al., 2022),

107   enabling the identification of potential BrC species by connecting them with light

108   absorption of OA. However, these approaches often output multi-dimensional data with

109   numerous variables, which must be evaluated appropriately. Traditional statistical

110   methods often perform poorly when handling large datasets and fail to accurately

111   elucidate complex interplays among variables (Fasola et al., 2020). Machine learning

112   (ML) is a powerful tool to effectively resolve such nonlinear relationships and address

113   issues of collinearity among variables (Tang et al., 2024). For instances, Zhang et al.

114   (2023) employed the Random Forest (RF) algorithm to quantify the factors driving

115    $PM_{2.5}$ trends in Tibetan Plateau from 2015 to 2022, revealing the importance of

116   anthropogenic emission reductions, and a similar ML approach was used for resolving

117   the driving factors of ozone pollution too (Zhu et al., 2024). Li et al. (2022b) applied

118   the ML-RF approach to analyze the sources of OA in submicron PM (PM_1) and $PM_{2.5}$,

119   showing the importance of secondary processes in supermicron PM. Wang et al. (2022a)

120   integrated the positive matrix factorization (PMF) with a multi-layer perceptron (MLP)

121   neural network to analyze the sources of BrC light absorption. Very recently, Wang et

122   al. (2024) applied the ML method to predict the optical properties of BrC with known

123   chromophores.

124   In this study, we conducted a systematic investigation on the chemical and optical

125   properties on the fine particular matter ($PM_{2.5}$) samples in both daytime and nighttime

126   collected in Nanjing, China during summer and cold seasons of 2022 ~ 2023.

127   Particularly, for the first time, we applied the ML-RF algorithm to connect the light-

128   absorbing characteristics with the determined organic molecules, aiming to identify

129   more unknown key BrC molecules. Our findings regarding the BrC properties,

130   especially the BrC molecules identified can be a good reference, and the ML application

131   can be an example of practice for future studies as well.

132

2 Experimental methods

2.1 Sampling site and sample collection

The $PM_{2.5}$ filter samples were collected in Nanjing, China, from July 11 to August 23, 2022, November 30 to December 10, 2022, February 13 to February 20, 2023, and March 3 to March 31, 2023. The first period represents the hot summer season (SS) (81 samples), and the later three periods represent the cold season (CS)(83 samples); note samples were not collected during precipitation in both seasons. The sampling site was located inside the campus of Nanjing University of Information Science and Technology (32°12'20.82"N, 118°42'25.46"E). The site was in a suburban area, surrounded by residential buildings, close to traffic arteries, and industrial zones (including chemical engineering, petrochemical, power plants and ironmaking and steelmaking plants).

A high volume sampler (Jinshida Ltd. Qingdao, China, model KB-1000) with a flow rate of $1.05 \ m^3 \ min^{-1}$ was employed. $PM_{2.5}$ samples were collected on the prebaked (450 ºC) quartz fiber filters (Pallflex, USA, size of 8 × 10 inch). Daytime samples were collected from 08:00 to 18:00 (Local Beijing time), and nighttime samples were collected from 19:00 to 07:00 on the next day. Each filter was wrapped in an aluminum foil and kept frozen at -20 °C until analysis. The concentrations of common gas pollutants (SO_2, NO_2, CO, and O_3) were obtained from the nearby National Environmental Monitoring Center (http://www.cnemc.cn/), while the meteorological parameters (air temperature, relative humidity, wind speed and direction) were recorded in the same site as $PM_{2.5}$.

2.2 Chemical analyses

2.2.1 Measurements of inorganic ions, organic carbon (OC) and elemental carbon (EC)

A number of round pieces (20 mm diameter) were punched from each sample filter, and were extracted by using 50 mL of ultrapure water (18.25 MΩ cm) (10 pieces) and

161   methanol (4 pieces), respectively. The filter pieces underwent 30 minutes of sonication

162   and were filtrated through the polytetrafluoroethylene (PTFE) syringe filters (0.22 μm)

163   to remove insoluble materials. Cations (NH_4^+, Na^+, K^+, Mg^{2+}, Ca^{2+}) were measured

164   using a 881 Compact IC Pro (Metrohm, Switzerland), anions (NO_3^-, SO_4^{2-}, Cl^-, F^-)

165   were determined by the ICS2100 (Dionex, USA). The water-soluble organic carbon

166   (WSOC) (μg C m^{-3}) was measured by a total organic carbon (TOC) analyzer (TOC-L,

167   Shimazu, Japan). Operational details of these analyses can be found in our previous

168   work (Chen et al., 2020a).

169   Concentrations of total elemental carbon (EC) and organic carbon (OC) in samples

170   were measured using a thermal optical carbon analyzer (RT-4; Sunset Laboratory, USA)

171   on a separate round filter piece (17 mm diameter) by using the IMPROVE TOT protocol

172   (Bai et al., 2020). In addition, the residual OC and EC contents in samples after

173   methanol extraction were determined with the same method above, and were subtracted

174   from the total OC content, to derive the methanol-soluble OC (MSOC) (μg C m^{-3}).

175   **2.2.2 Bulk analysis of organics**

176   We employed specially an Aerodyne soot particle AMS (SP-AMS) to determine

177   the bulk composition of water-soluble OA (WSOA) (Onasch et al., 2012). It should be

178   noted that, direct AMS analysis on the methanol-soluble OA (MSOA) is currently

179   unfeasible, even though it might be more important than WSOA in both concentration

180   and light absorption. Likewise almost all offline AMS analysis methods (O'brien et al.,

181   2019; Vasilakopoulou et al., 2023), this is due to that the methanol solvent and its

182   associated organic impurities cannot be effectively removed, making the obtained

183   MSOA signals unidentifiable.

184   The analysis procedure of WSOA is similar to that described in Ge et al. (2017). In

185   brief, eight round pieces (20 mm diameter) of each filter were sonicated in 40 mL of

186   ultrapure water, and the aqueous extract was nebulized using an atomizer (TSI, Model

187   3076), then the mist was dried by a silica gel diffusion dryer and the remaining particles

188   were sent to the SP-AMS. The SP-AMS was operated in a laser-off mode, therefore it

189   measured non-refractory species that can be rapidly vaporized at 600 °C (SP-AMS oven

190 temperature). Note the SP-AMS employs a 70 eV electron impact (EI) ionization

191 scheme, so the vaporized species are fragmented into positively charged ions with

192 different mass-to-charge (m/z) ratios and we obtained the composition of WSOA in the

193 form of lumped molecular fragments rather than detailed molecular composition.

194   The SP-AMS data were post-processed using the Igor-based ToF-AMS analysis

195 toolkit (SQUIRREL version 1.56D and PIKA version 1.15D). Elemental ratios

196 including hydrogen-to-carbon (H/C), oxygen-to-carbon (O/C) and nitrogen-to-carbon

197 (N/C) as well as the organic mass to organic carbon (OM/OC) ratio were calculated by

198 using the methods proposed in Aiken et al. (2008), Canagaratna et al. (2015) and Ge et

199 al. (2024). The WSOA mass concentration of each sample was normalized by

200 multiplying the WSOC concentration with its corresponding OM/OC. Then, we

201 conducted the PMF analysis to resolve the sources of WSOA by utilizing the PMF

202 evaluation toolkit (Version 2.06) (Ulbrich et al., 2009), followed strictly the protocol

203 described in Zhang et al. (2011). As usual, we included only ions with $m/z \leq 120$, and

204 PMF solutions were explored by varying the number of factors (from 3 to 8) and

205 rotation parameters (f_{peak}, from -1 to 1 with an increment of 0.2). Based on the

206 diagnostic plots in Fig. S1 in the supplement, the four-factor solution was selected as

207 the best solution. The factors include a hydrocarbon-like OA (HOA) relevant with fossil

208 fuel combustion, a biomass burning-related OA (BBOA), a less oxidized oxygenated

209 OA (OOA1) and a more oxidized oxygenated OA (OOA2) (see details in Sect. 3.1.2).

210   **2.2.3 Molecular characterization of organics**

211   Molecular-level characterization of organic species was conducted by using an

212 ultra-high performance liquid chromatography with a quadrupole time-of-flight (QTOF)

213 mass spectrometer (UPLC-QTOF-MS) (ACQUITY UPLC H-Class coupled with a

214 Xevo G2-XS QTOF, Waters). The sample pretreatment was described in Text S1, and

215 the analyzed organics are those dissolved in methanol (namely MSOA). Compound

216 separation was performed with a Luna Omega 1.6 μm C18 column (100 mm × 2.1 mm

217 × 1.6 μm), and the sample aliquot was subjected to electrospray ionization (ESI), and

218 detected in both positive and negative ion modes. The scanning m/z range for each mass

219   spectrum was 50-1200, with a scanning rate of one spectrum per 0.1 second. More

220   details are presented in Text S2.

221   The original UPLC-QTOF-MS data were processed using the Mass Spectrometry-

222   Data Independent Analysis (MS-DIAL, version 4.92) software (Tsugawa et al., 2015),

223   including peak extraction, alignment and deconvolution, achieving a detection

224   probability of 70% in all samples for any identified compound. The method of

225   systematic error removal using random forest (SERRF, a ML algorithm), was then

226   introduced to reduce systematic errors and normalize the measured data (Fig. S2). All

227   deconvoluted spectra were imported into the SIRIUS (Version 5.6.2) toolkit (Dührkop

228   et al., 2019) to determine molecular formulas. The semi-quantitative concentrations of

229   identified molecules were expressed in the normalized peak areas (NPRs), defined as

230   their peak areas acquired from SERRF divided by air volumes of the samples.

231   In addition, the double-bond equivalent (DBE) was used to indicate the level of

232   unsaturation of the compound (Bae et al., 2011), and the aromaticity equivalent (Xc)

233   (Yassine et al., 2014) was used to indicate the molecular structure. O/C, H/C and DBE

234   values of the sample were averaged over all identified molecules based on their relative

235   abundances (See details in Text S3).

236

237   **2.3 Optical analyses**

238   **2.3.1 Light absorption properties**

239   The light absorption spectra of both WSOC and MSOC in 200 ~ 800 nm were

240   obtained using a UV-Vis spectrophotometer (UV-3600, Shimadzu, Japan) with a 0.5 nm

241   interval. The absorbance at a certain wavelength λ (A_λ) were corrected by subtracting

242   that at 700 nm (A_{700}) (near zero, as background), and the corresponding light absorption

243   coefficient (Abs_λ, M m^{-1}) is calculated as below (Hecobian et al., 2010):

244
$$Abs_\lambda = (A_\lambda - A_{700}) \times \frac{V_l}{V_a \times L} \times \ln(10) \qquad (1)$$

245   Where V_l represents volume of the extract (water or methanol), V_a denotes air

246   volume of the filter piece, and L is the optical path length (0.01 meters here).

247   The corresponding mass absorption efficiency (MAE_λ, m^2 g^{-1}) can then be

248 calculated below:

$$\text{MAE}_\lambda = \frac{\text{Abs}_\lambda}{[\text{WSOC}] \ ([\text{MSOC}])} \qquad (2)$$

250 Where [WSOC] ([MSOC]) represents the mass concentration of WSOC (MSOC).

251 Following previous studies (Laskin et al., 2015; Chen et al., 2018; Xie et al., 2020;

252 Chen et al., 2020b), the light absorption at 365 nm (Abs_{365}) was employed as a surrogate

253 for BrC in this work.

254 The relationship between the Absorption Ångström Exponent (AAE)(an index of

255 the wavelength dependence) (Andreae and Gelencsér, 2006) and light absorption is

256 shown below:

$$Abs_\lambda = K \cdot \lambda^{-AAE} \qquad (3)$$

258 Where K is a constant related to light absorption, and we computed the AAE values

259 in the $300 \sim 450$ nm range.

260 Additionally, a multi-linear regression (MLR) method was used to estimate the

261 contributions of different WSOA factors to the light absorption of total WSOA, as

262 shown in the following equation :

$$\text{Abs}_{365,\text{WSOC}} = a \times \text{HOA} + b \times \text{BBOA} + c \times \text{OOA1} + d \times \text{OOA2} \qquad (4)$$

264 Here, HOA, BBOA, OOA1, and OOA2 represent time series of the WSOA factors. a,

265 b, c, and d are the fitting parameters, which are the mass absorption efficiency (MAE)

266 values of corresponding factor.

267 The direct radiative forcing effect of BrC can be represented by the simple forcing

268 efficiency (SFE) (in W g^{-1}), which is the energy added to the earth-atmosphere system

269 per unit mass of aerosol (Bond and Bergstrom, 2006). The SFE of BrC at the

270 wavelength λ can be expressed below (Chen and Bond, 2010):

$$\frac{\text{dSFE}}{\text{d}\lambda} = -\frac{1}{4}\frac{\text{dS}(\lambda)}{\text{d}\lambda}\tau_{\text{atm}}^2(\lambda)(1 - F_C)$$
$$[2 \times (1 - \alpha_S)^2\beta(\lambda)\text{MSE}(\lambda) - 4 \times \alpha_S \times \text{MAE}(\lambda)]\text{d}\lambda \qquad (5)$$

272 Where $S(\lambda)$ represents the solar irradiance at λ obtained from the ASTM G173–03

273 reference spectra. τ_{atm} denotes the atmospheric transmission (0.79), F_C is set to 0.6,

274 indicating the fraction of cloud cover, the global average value of α_s is fixed at 0.19,

275 representing the surface albedo, β is the backscatter fraction, and MSE and MAE are

276   the mass scattering efficiency and mass absorption efficiency of BrC, respectively. .

277   When estimating the radiative effect of BrC, the direct radiative forcing caused by

278   aerosol scattering can be neglected. Therefore, the absorbed radiative forcing within a

279   given spectral range is calculated by the simplified Eq. (6):

280
$$\text{SFE} = \int \frac{dS(\lambda)}{d_\lambda} \tau_{atm}^2(\lambda)(1 - F_C) \times \alpha_S \times \text{MAE}(\lambda) \, d\lambda \qquad (6)$$

281   **2.3.2 Fluorescence properties**

282   Characterization of excitation-emission matrix (EEM) of the extracts was

283   performed using a fluorescence spectrophotometer (Cary Eclipse, Agilent, USA) The

284   wavelength range of excitation was set from 230 to 500 nm, and that of emission was

285   from 250 to 600 nm, the scanning resolutions of excitation and emission were 5 nm and

286   2 nm, respectively, with the scanning speed of 1200 nm min^{-1}. The photomultiplier tube

287   (PMT) detector voltage was set at 600 V. The measurement was subjected to instrument

288   calibration, internal filter correction, Raman/Rayleigh scattering correction, and all

289   EEM spectra were subjected to blank filter subtraction. The processed data were further

290   analyzed using PARAFAC to group potential components with similar fluorescent

291   properties. The analysis was performed using MATLAB 2022b software with the

292   drEEM toolbox (Murphy et al., 2013).

293   Fluorescent properties of the extracts were also characterized by the humification

294   index (HIX), biological index (BIX), and fluorescence index (FI). HIX is defined as the

295   ratio of integrated fluorescence emission intensity in the range of 435 - 480 nm to that

296   in the range of 300 to 345 nm when excited at 254 nm; BIX is calculated as the ratio of

297   emission intensity at 380 nm to that of 430 nm for the excitation wavelength of 310 nm;

298   FI is the ratio of emission intensity at 470 nm to that of 520 nm under a fixed 370 nm

299   excitation wavelength (Birdwell and Engel, 2010; Mcknight et al., 2001).

300

301   **2.4 Machine learning identification of key light-absorbing species**

302   The ML RF model was used here to screen the key light absorbing species by

303   linking the target variable (Abs$_{365}$) with the identified organic molecules (in NPRs), via

304   the "randomforest()" function in R software (Version 4.3.2). Note both light absorption

305   and organic molecules are for MSOA. The model included 500 decision trees and

306   estimated the variance through a cross-validation during training. The dataset was

307   divided into a training set (80% of total) and a test set (20% of total) to assure accuracy

308   and robustness of the model.

309   The model outputted two key indices to assess the importance of each molecule to

310   the light absorption. One metric is IncNPu_val, which can measure the purity of nodes.

311   During the construction of each tree in the RF model, each split can increase the purity

312   of nodes, therefore if more frequently a variable is used in splitting, more contribution

313   it has to the increase of purity of nodes, then the variable is considered to be important.

314   IncMSE_val is another index based on the mean squared error (MSE). When we

315   permute a variable, increase in the projected error can serve as a measure of its

316   importance. If a variable with a significant impact on the predicted results is permuted,

317   the model's MSE would increase significantly, resulting in a high IncMSE_val value

318   (González et al., 2015). Under the 50th percentile of IncMSE_val, some variables had

319   zero or even negative contributions to IncMSE_val. Considering the definition of

320   IncMSE_val, such variables would have either no or negative influence on model fitting,

321   thus only the top 50 % of compounds were chosen. Afterwards, intersection of the two

322   indices were considered as potential BrC chromophores.

323   Moreover, a molecule typically requires a substantial uninterrupted conjugation on

324   its molecular backbone to effectively absorb visible light (Lin et al., 2018), therefore a

325   compound with the ratio of DBE to carbon (DBE/C) greater than that of linear polyenes

326   (with a molecular formula of C_xH_{x+2}, DBE/C = 0.5) (Cain et al., 2014) is treated as a

327   potential BrC compound. Besides, the DBE/C ratio should be less than the upper limit

328   of DBE for natural compounds (DBE/C = 0.9) (Lobodin et al., 2012). Finally, the

329   candidate compounds passed aforementioned criteria were compared with those in

330   open-source databases, including MoNA (https://mona.fiehnlab.ucdavis.edu/) and

331   MassBankEU (https://massbank.eu/), to be interpreted as the key BrC compounds.

332

3 Results and discussion

3.1 Chemical properties

3.1.1 General characteristics

During the sampling period, the temperatures were 34.34 ± 3.23 °C (daytime) ($\pm$ one standard deviation, hereinafter) and 30.85 ± 2.97 °C (nighttime) during SS, 13.00 ± 6.04 °C (daytime) and 9.97 ± 5.04 °C (nighttime) during CS, and the relative humidity (RH) levels were 53.61 ± 10.33 % (daytime) and 65.88 ± 9.87 % (nighttime) during SS, 47.81 ± 18.94 % (daytime) and 55.56 ± 15.74 % (nighttime) during CS, respectively (Figs. 1a and b). Figure 1c depicts the temporal variations of different components. Average concentrations of OC, EC, WSOC, MSOC and total ionic species during daytime and nighttime in the two seasons are summarized in Table 1. Clearly, concentrations of all components were higher in CS than those in SS, but the daytime/nighttime differences were relatively small in both seasons. Also, the MSOC levels were larger than WSOC in all samples. MSOC occupied 82.4 % and 81.5 % while WSOC occupied 61.3 % and 49.5 % of the total OC during SS and CS, respectively, indicating that methanol can more effectively extract the aerosol organics than water.

The mean mass contributions of different ions to their total during SS and CS, respectively are shown in Fig. 1c too. The particles were overall neutral as the molar ratios of inorganic anions to cations were 0.97 and 0.98 during SS and CS, respectively (Fig. S3). The most abundant ion was sulfate in SS (45.5 %) and nitrate in CS (50.7 %), as low temperatures during CS favor the partitioning of nitrate to particle phase. As so, the sulfur oxidation ratio (SOR, $[SO_4^{2-}]/([SO_4^{2-}]+[SO_2])$) and nitrogen oxidation ratio (NOR, $[NO_3^-]/([NO_3^-]+[NO_2])$) were 0.58 and 0.16 (daytime) and 0.56, 0.17 (nighttime) during SS, 0.40, 0.28 (daytime) and 0.42, 0.30 (nighttime) during CS, respectively. NOR was indeed much higher in CS especially during nighttime than those in SS. Furthermore, ammonium (NH_4^+) was the predominant cation while sulfate, nitrate and chloride were major anions. The scatter plots of molar concentrations of ammonium versus summed sulfate, nitrate and chloride (Fig. S4) reveal different bonding forms of the aerosol inorganic salts in different seasons. The correlations were both tight

362 (correlation coefficients close to 1) yet the fitted slopes during SS were 0.80 (daytime)

363 and 0.89 (nighttime) while those during CS were 0.98 (daytime) and 0.99 (nighttime),

364 respectively. Such results demonstrate that ammonium was deficit to neutralize the

365 cations therefore significant amounts of metal salts (such as sodium/calcium

366 sulfate/nitrate) could exist during SS while during CS, most inorganic species were in

367 the forms of $(NH_4)_2SO_4$, NH_4NO_3 and NH_4Cl with no appreciable metal salts.

368 **3.1.2 Features and sources of water-soluble organics**

369 Regarding the water-soluble portion of organic species (WSOA), Figure 2a

370 presents the average high resolution mass spectra (HRMS) during SS and CS,

371 respectively. It can be seen that, WSOA during CS appeared to be much more

372 oxygenated than that during SS (O/C: 0.58, 0.59 vs. 0.44, 0.45) . To further unravel

373 causes of such differences, PMF analysis were conducted and the HRMS of resolved

374 factors are presented in Fig. 2b, while mass contributions of these factors during SS and

375 CS as well as the Pearson's correlation coefficents (r) of these factors with other

376 components are illustrated in Fig. 3.

377 The HOA MS was dominated by $C_xH_y^+$ ions (57.2 %), such as $C_4H_7^+$ (m/z 55) and

378 $C_4H_9^+$ (m/z 57), primarily originating from hydrocarbons emitted from fossil fuel

379 combustion (such as traffic) (Canagaratna et al., 2004). Among the four factors, HOA

380 exhibited the lowest O/C ratio (0.24) and the highest H/C ratio (1.66). This is consistent

381 with the behaviors of HOA from a number of previous offline AMS studies

382 (Daellenbach et al., 2017; Liu et al., 2021; Ye et al., 2017; Qiu et al., 2019). The second

383 factor was identified as BBOA, since it has distinct peaks at m/z 60 (mainly $C_2H_4O_2^+$,

384 0.76 % of the total HRMS) and m/z 73 (mainly $C_3H_5O_2^+$, 1.09 % of the total HRMS),

385 which are characteristic fragments associated with levoglucosan, a tracer compound of

386 biomass burning particles (Kumar et al., 2022; Qin et al., 2017). Correlations between

387 BBOA and these two tracer ions were indeed tight (0.71 with $C_2H_4O_2^+$and 0.82 with

388 $C_3H_5O_2^+$). A notably positive correlation between BBOA and K^+ (Fig. 3b) further

389 supports its BB origin as K^+ is also a common BB emission tracer (Yu et al., 2018).

390 Note the BBOA here had a relatively higher O/C ratio of 0.61 than those identified in

391 previous offline AMS measurements, such as Yangzhou (0.45) (Ge et al., 2017), Beijing,

392 China (0.59) (Qiu et al., 2019), and Marseille, France (0.54) (Bozzetti et al., 2017),

393 suggesting the presence of partially aged BBOA species in this factor.

394   The other two factors are secondary. OOA1 was less oxidized with a O/C of 0.39

395 and OOA2 was more oxygenated with the highest O/C of 0.65 among all factors. OOA1

396 had characteristic fragments at m/z 29 (CHO^+) and m/z 43 (mainly $C_2H_3O^+$) while

397 OOA2 had the least fraction of oxygen-free $C_xH_y^+$ ions (28.5 %) but the largest fraction

398 of oxygenated ions (32.8 % of $C_xH_yO_1^+$ and 18.9 % of $C_xH_yO_2^+$) among the four factors.

399 OOA2 correlated well with CO_2^+ (m/z 44) (r of 0.81), a characterisitic ion of highly

400 oxygenated carboxylic/dicarboxylic acids. Moreover, OOA2 had the highest N/C of

401 0.095 as well as those of $C_xH_yN^+$ (9.1 %) (such as CH_2N^+, CHN^+ and CH_4N^+) and

402 $C_xH_yO_zN^+$ (3.8 %) (such as $CHON^+$, CH_2NO^+ and CH_4NO^+), indicating the presence of

403 amines and amino acids correspondingly (Ge et al., 2024). Besides, the N/C level of

404 OOA2 is close to that of fogwater observed in Fresno, indicating the aqueous phase

405 reactions are likely an source of those nitrogen-containing ions in OOA2 (Kim et al.,

406 2019). In addition, sulfur-containing organic ions (such as CH_2S^+, $CH_3SO_2^+$ and CHS^+)

407 were almost exclusively present in OOA2 and in a significant fraction (2.7 %), as such

408 ions were strongly associated with aqueous/heterogenous reactions (Zorn et al., 2008;

409 Huang et al., 2020; Petters et al., 2021; Mcneill, 2015), reassuring that OOA2 was very

410 likely linked with aqueous/heterogenous formation pathway.

411   The time series of mass contributions of the four factors are shown in Fig. 1d, and

412 significant differences can be observed during the two sampling seasons, as can be seen

413 clearly in Fig. 3a. HOA was a significant source in both SS and CS, and as expected, it

414 was higher during daytime due to the stronger traffic activities. BBOA was much less

415 important than HOA, but its contribution during CS was obviously more than that

416 during SS (12.5 ~ 13.0 % vs. 7.2 ~ 7.8 %), and accordingly, HOA contribution was

417 slightly larger during SS than during CS (38.0 ~ 41.7 % vs. 29.9 ~ 36.8 %). It is worthy

418 to mention that, BBOA can be more important than HOA, such as in Bejing during

419 autumn polluted period (38.3% of WSOA) (Hu et al., 2020) , in Delhi, India (31-34%

of WSOA) (Bhowmik et al., 2024), and in urban and rural Catalonia, Spain (up to 26% of WSOA) (Veld et al., 2023). In general, the dominance of SOA in WSOA observed here was consistent with most offline AMS studies aforementioned, except that POA was found to dominate WSOA in Delhi, India (Bhowmik et al., 2024). However, mass contributions of the two individual SOA factors in different seasons in this study were strikingly different. OOA1 occupied nearly half of the total WSOA (47.5 ~ 49.8 %) while contributions of OOA2 were only 3.0 ~ 5.0 % during SS; on the other hand, OOA2 occupied 38.6 ~ 43.5 % of WSOA mass while those of OOA1 were down to 11.6 ~ 14.1 %. The much larger OOA2 fraction during CS explains its overall high oxidation degree depicted in Fig. 2. These results are well consistent with our previous studies, as we show that during summer in Nanjing, photochemical reactions dominate the SOA formation and yield relatively less oxygenated OA (Xian et al., 2023; Wang et al., 2022b), while during cold seasons, aqueous formation of SOA becomes more important which can generate highly oxygenated OA (Wu et al., 2018). The air temperature (a solar radiation indicator) and ozone (a photochemical product) both correlated positively with OOA1 but negatively with OOA2 (Fig. 3b), further verifying the dominance of photochemical production of OOA1 not OOA2. As is well known, particulate nitrate was strongly associated with heterogenous reactions and gas-to-particle partitioning favored by low temperature and high RH especailly during CS, and indeed, OOA2 correlated much tighter with NH_4NO_3 than OOA1 did.

3.2 Optical properties

3.2.1 Light-absorbing properties of WSOC and MSOC

The average light absorption coefficients of BrC in WSOC and MSOC in 300 ~ 700 nm during daytime and nighttime of SS and CS are illustrated in Fig. 4a. As expected, the values all exponentially decreased as a function of wavelength. The calculated AAE values are listed in Table 1. It is interesting to find that the WSOC AAE had no significant difference between SS and CS (6.35 vs. 6.43), while that of MSOC AAE appeared to be notable (5.99 vs. 6.89); Compared with the MSOC AAE, the

449   WSOC AAE was higher during SS but smaller during CS. The AAE values obtained

450   here are slightly smaller than those reported in Beijing (7.3 ~ 7.5 of WSOC) (Du et al.,

451   2014; Chen et al., 2016), comparable to that in Guangzhou (6.7 of WSOC) (Fan et al.,

452   2016). Note Chen and Bond (2010) reports that particles generated from smoldering of

453   various types of wood exhibit a AAE of 6.9 ~ 11.6 (MSOC); Lambe et al.(2013) shows

454   that lab-generated secondary BrC possesses a AAE of 5.2 ~ 8.8 (MSOC). Compared

455   with these values, our measured AAE values (<7) here probably suggest a dominance

456   of secondarily formed BrC for both WSOC and MSOC. This can be verified by Fig. 3a

457   for WSOC, as indeed it was dominated by SOA particularly during nighttime in both

458   seasons. However, the large difference in WSOA chemical composition in different

459   seasons (especially SOA proportions) did not result in a large difference in WSOC AAE,

460   demonstrating clearly the non-correspondence of chemical species to light-absorbing

461   species (a.k.a., BrC). On the contrary, for MSOC, the relatively large difference of

462   MSOC AAE in different seasons likely reflect the distinction of BrC species but not

463   necessarily chemical constitution. The light absorption coefficients at 365 nm (Abs_{365})

464   are listed in Table 1 too. The average $Abs_{365, WSOC}$ during CS (4.87 M m^{-1}) was

465   approximately 2.15 times that of SS (2.27 M m^{-1}), and that of MSOC during CS (4.97

466   M m^{-1}) was also much larger than that during SS (3.64 M m^{-1}); Nighttime values were

467   higher than those in daytime expect for WSOC during CS. For the same set of samples,

468    $Abs_{365, MSOC}$ values were typically larger than $Abs_{365, WSOC}$ except that CS daytime

469    $Abs_{365, MSOC}$ was slightly smaller than $Abs_{365, WSOC}$ (4.65 vs. 4.89 M m^{-1}). Scatter plots

470   of Abs_{365} versus WSOC (and MSOC), and $Abs_{365, WSOC}$ versus $Abs_{365, MSOC}$ for the four

471   series of samples are given in Fig. S5. The correlations were generally well especially

472   those of WSOC and MSOC ($r > 0.80$), suggesting that there is a large overlap of

473   extracted species between WSOC and MSOC, as well as their BrC constituents.

474   Regarding the MAE at 365 nm (MAE_{365}), $MAE_{365, WSOC}$ during CS (0.75 m^2 g^{-1})

475   was higher than that during SS (0.55 m^2 g^{-1}), indicating its stronger light absorption

476   ability during CS; however, the $MAE_{365, MSOC}$, unlike $Abs_{365, MSOC}$, was smaller during

477   CS than that during SS (0.50 vs. 0.72 m^2 g^{-1}). Besides, MAE_{365} values for both WSOC

and MSOC were slightly larger during nighttime than those during daytime in both seasons. Compared to previous winter studies, the $MAE_{365, WSOC}$ in Nanjing here was lower than that in Beijing (1.21 ~ 1.26 m^2 g^{-1}) (Du et al., 2014; Chen et al., 2016; Li et al., 2020), similar to our earlier observation in Yangzhou (0.75 m^2 g^{-1}), but the $MAE_{365, MSOC}$ appears to be less than that in Yangzhou (1.12 m^2 g^{-1})(Chen et al., 2020). To further explain the low MAE_{365} observed here, we investigated the air mass origins of our samples collected in different periods via back trajectory analysis (at an altitude of 200 m and 24 hours backwards) using the MeteInfo (Version: 3.0.0) (Wang, 2019). As shown in Fig. S6, only a limited fraction of air mass trajectories passed through sea and coastal areas (clusters 4 and 5, 27.05 % during daytime and 29.54 % during nighttime) during SS, while during CS, proportions of trajectories that intercepted sea/costal air increased to 79.80 % (clusters 1, 2 and 3 during daytime) and 69.44% (clusters 2, 3 and 4 during nighttime), respectively. Note the air masses during CS are somewhat unusual as typically they mainly originate from inland regions (Wu et al., 2019b), which might cause the low MAE_{365} observed in this work as particles affected by marine air can be less light-absorptive than those influenced by inland air (Li et al., 2022a).

Saleh (2020) proposes a method that uses the MAE_{405} (MAE at 405 nm) – AAE two-dimension space to assess the light-absorbing ability of BrC, as shown in Fig. 4b. The majority of samples in this study fall into the regime of W-BrC (weakly light-absorptive BrC) with a few MSOC samples locating in the VW-BrC (very weak BrC) regime, which are similar to a few other observations (Zhou et al., 2021; Xu et al., 2022). The BrC in MSOC seemed to cover a broader region than it in WSOC, indicating that the MSOC BrC might contain a wider array of species and/or originate from more diverse sources/processes. Daytime/nighttime difference of MSOC BrC was also more obvious than that of WSOC BrC.

At last, we estimated the SFE values of WSOC and MSOC in the range of 300–700 nm, considering the actual visible light wavelength as well as the negligible light absorption above 700 nm of BrC. As summarized in Table 1, the mean SFE_{MSOC} (2.43 W g^{-1}) during SS was higher than that of WSOC (2.20 W g^{-1}), but it became smaller

507 during CS (2.23 W g^{-1}) and was much lower than that of WSOC (3.24 W g^{-1}). The

508 SFE$_{WSOC}$ values in both SS and CS were lower than that in Beijing (4.6 ± 1.7 W g^{-1} in

509 summer and 6.2 ± 2.0 W g^{-1} in winter), especially in CS (Deng et al., 2022). For both

510 WSOC and MSOC, SFE values during nighttime were slightly larger.

511 **3.2.2 Source apportionment of light absorption of WSOC**

512 In Sect. 3.1.2, sources of WSOA were identified and quantified, herein we applied

513 a multiple linear regression (MLR) algorithm to apportion the light absorption of

514 WSOC to these sources. The scatter plot of reconstructed Abs$_{365, WSOC}$ versus measured

515 values are shown in Fig. S7. The fitted slope is 1.06 with a Pearson's *r* of 0.90, verifying

516 the robustness of this method on our dataset. The calculated regression coefficients,

517 representing the factors' MAE$_{365}$ values (m^2 g^{-1}) are listed in Table 2. Compared to our

518 earlier results (Chen et al., 2020b), the HOA MAE$_{365}$ (0.71 m^2 g^{-1}), was much less than

519 that in Yangzhou (1.46 m^2 g^{-1}), while the BBOA MAE$_{365}$ values were similar (0.71 vs.

520 0.77); MAE$_{365}$ values of OOA1 (0.12 m^2 g^{-1}) and OOA2 (0.83 m^2 g^{-1}) were very close

521 to the two SOA factors in Yangzhou (0.11 and 0.85 m^2 g^{-1}). However, here the less

522 oxygented OOA1 has the small MAE$_{365}$ while in Yangzhou, the more oxygenated SOA

523 has the similar MAE$_{365}$ as OOA1, and *vice versa* for the other pair. This work finds that

524 the more oxidized SOA has a stronger light absorption ability, opposite to that reported

525 in Yangzhou. Nevertheless, the two findings are not contradictory with each other, as

526 atmospheric ageing can lead to either photo-enhancement or photo-bleachment,

527 dependent upon the precursors. For instances, aqueous oxidation of BBOA can increase

528 (Gilardoni et al., 2016) yet conversely aqueous processing of fossil fuel combustion OA

529 can decrease the light absorptivity of OA (Wang et al., 2021). As discussed in Sect.

530 3.2.1, the unusual air masses during CS in this work clearly indicate different precursors

531 from those in Yangzhou.

532 The average contributions of HOA, BBOA, OOA1 and OOA2 to Abs$_{365, WSOC}$

533 across the whole campaign were 33.05 %, 15.49 %, 6.00 % and 45.46 %, respectively

534 (Table 2). Figure 5 further presents contributions of the factors under different scenarios.

535 Compared with their mass contributions shown in Fig. 3a, during SS, the dominant

contributor of light absorption became HOA (daytime 63.7 %, nighttime 55.6 %), and contributions of BBOA and OOA2 both increased relative to their mass fractions; while OOA1's contribution was largely reduced to 15.0 ~ 16.2 % due to its small MAE_{365}. Previous studies have consistently identified coal combustion (Fan et al., 2016; Li et al., 2019; Song et al., 2019) and traffic emissions (Hecobian et al., 2010) as significant contributors to BrC, together with our results here, highlighting the substantial impact of anthropogenic fossil fuel combustion on atmospheric visibility. During CS, OOA2 dominated the light absorption (daytime 50.7 %, nighttme 63.0 %) owing to its large mass contribution as well as large MAE_{365}; OOA1 became a very minor contributor (2.1 ~ 2.8 %), HOA contribution decreased while BBOA contribution increased relative to their mass fractions. Overall, we find that primary fossil fuel combustion emissions govern water-soluble BrC light absorption during SS especailly during daytime, while during CS, secondary highly aged species (likely from aqueous/heterogenous reactions) dominates, especially during nighttime.

To further explore the impact of atmospheric ageing on BrC, we plotted MAE_{365} as a function of O/C in Fig. 6. Interestingly, during SS, MAE_{365} generally decreased with the increase of O/C, especially in daytime as its fitted slope of -1.56 was over 2 times that of nighttime (-0.76). On the other hand, MAE_{365} showed an increasing trend against O/C during CS, particularly in nighttime as the fitted slope was 1.43, larger than that of daytime (1.12). These results further supports our earlier findings and underscore that during summer photochemical reactions can lead to photo-bleachment of aerosols while during cold seasons aqueous/heterogenous reactions might dominate the secondary formation and lead to photo-enhancement; clearly, photochemical oxidation and aqueous/heterogenous reactions are more active during daytime and nighttime, respectively, consistent with the slopes in Fig. 6. Also, photochemcially produced SOA was often less or moderately oxygenated and that from aqueous/heteregenous oxidation was more oxidized, and there is a turning point at O/C of 0.45 ~ 0.5 in the MAE_{365}-O/C plot. Many studies have shown that aqueous reactions are a source of BrC (e.g., Li et al. (2022c), Laskin et al. (2015) and Ye et al. (2019)), but evidence also shows that

565 further aqueous ageing of BrC can lead to photo-bleaching (e.g., Zhao et al. (2015) and

566 Lei et al. (2025)), therefore a certain O/C turning point can exist if the OA evolution

567 was governed by a certain process. The real atmospheric processes are however

568 complicated, such O/C points might be less clear. Nevertheless, similar points were

569 indeed observed previously (Zhong et al., 2023; Jiang et al., 2022).

570 **3.2.3 Fluorescent properties of WSOC and MSOC**

571 The fluorescence indices like HIX, BIX and FI, can infer the types and sources of

572 dissolved organic matter (DOM) in aquatic systems and soils (Lee et al., 2013; Huguet

573 et al., 2009). Recently, these indices have been employed to investigate sources and

574 aging processes of atmospheric OA (Fu et al., 2015; Qin et al., 2018; Deng et al., 2022;

575 Murphy et al., 2013). Here, we calculated these indices for both WSOC and MSOC.

576 HIX represents the degree of humification, and a high HIX means high

577 aggregation, C/H ratio and aromaticity of the organics (Zsolnay et al., 1999; Mcknight

578 et al., 2001; Birdwell and Engel, 2010), thus it normally increases upon ageing (Fan et

579 al., 2019; Murphy et al., 2013). In this study, HIX of WSOC during SS and CS were on

580 average 3.34 and 4.68, respectively (Table 3), much less than the HIX levels in aquatic

581 or soil DOM (Dong et al., 2017), suggesting an overall low aromaticity of atmospheric

582 OA in Nanjing. As a comparison, the WSOC HIX are higher than those in Colorado,

583 USA (2.42) (Xie et al., 2016) and Tianjin, China (2.73 and 2.22) (Deng et al., 2022),

584 but significantly lower than that in Nanjing during 2017-2018 (7.07) (Xie et al., 2020).

585 An earlier study proposes the HIX ranges of 1.4-5 for fresh SOA and 4.2-6.1 for aged

586 SOA (Lee et al., 2013). Despite influences of other primary sources, the average HIX

587 during SS did fall in the fresh SOA range and the value during CS entered the edge of

588 aged SOA, in line with the oxidation degrees of OA (Fig. 2a) and mass proportions of

589 fresh/aged SOA factors (namely, OOA1/OOA2) (Fig. 3a) during different seasons. The

590 average HIX of MSOC (2.72 and 3.48) were lower than those of WSOC in both seasons,

591 indicating that HULIS with high aromaticity are preferentially soluble in water.

592 FI is indicative of the relative contributions of terrestrial and biogenic sources

593 while BIX, in contrast to HIX, can be treated as a freshness index. A fluorophore is

often associated with high aromaticity if FI is low (Fu et al., 2015), and a high BIX indicates a high content of freshly released organics (such as biological or microbial derived species) (Wen et al., 2021; Huguet et al., 2009; Murphy et al., 2013). The average WSOC BIX values during SS and CS were determined to be 0.84 and 0.88, respectively, with corresponding FI of 1.91 and 1.90 (Table 3), and the corresponding MSOC BIX were 0.90 and 0.96, and MSOC FI were 2.27 and 2.11, respectively. Compared with results during 2017-2018 in Nanjing, BIX and FI values of WSOC were similar, yet those of MSOC here were larger (Xie et al., 2020). Figure 7 shows the measured data in the HIX-FI and HIX-BIX diagrams along with results from a few other studies. It can be seen that, almost all BIX values distributed in the range of 0.6 ~ 1 (Huguet et al., 2009) and FI values distributed within 1.6 ~ 1.9 (Mcknight et al., 2001), suggesting that OA in both seasons was influenced by a mix of terrestrial and microbial/biogenic sources. For both WSOC and MSOC, BIX was slightly higher during CS than during SS, attributing to the fact that OA during CS contained more aged SOA species. Nearly no difference for WSOC FI during different seasons were observed, but the MSOC FI during CS was slightly lower than that during SS, meaning that MSOC during CS had a high aromaticity as expected. In addition, BIX and FI values during nighttime were marginally higher than those during daytime in all cases.

3.2.4 Identification of key fluorophores of WSOC and MSOC

The 3D EEM-PARAFAC analysis was adopted to identify the key fluorophores of BrC, with results in Fig. 8 and Fig. S8. Four components were resolved for both WSOC and MSOC. For WSOC, C1 exhibited a peak at Ex = 230 nm and Em = 374 nm, identified as less oxidized HULIS typically associated with combustion sources. Its contribution was only 4.9 % during SS but increased to 19.2 % during CS (Fig. S8a). C2 had a prominent peak at Ex = 230 nm and Em = 396 nm and a second peak at Ex = 320 nm and Em = 396 nm, classified as a HULIS-related component too, as the dual-peak distribution of fluorescence spectrum is often associated with HULIS (Coble, 1996; Murphy et al., 2011; Yu et al., 2015); its second peak indicates the abundance of compounds with condensed aromatics, conjugated bonds, and non-linear rings (Matos

623   et al., 2015), likely a mix of primary and secondary sources. C2 contribution was thus

624   comparable during different seasons (37.5 % vs. 38.6 %), and it seemed to be more

625   important in nighttime than in daytime (44.0 % vs. 26.9 % during SS, and 41.4 % vs.

626   34.8 % during CS). C3 component, with a peak at Ex = 240 nm and Em = 446 nm, was

627   considered as a highly oxidized HULIS component, relevant with secondary processes

628   (Cheng et al., 2016; Cao et al., 2021). Hawkins et al. (2016) and Aiona et al. (2017)

629   reported fluorescent pattern of products from aqueous-phase reaction of aldehydes with

630   ammonium sulfate or amines (Ex < 250/300 nm and Em > 400 nm) well matching the

631   pattern identified here. As discussed earlier, aqueous/heterogenous reactions

632   contributed to WSOA, especailly during CS; correspondingly, C3 contribution was

633   indeed much higher during CS than during SS (24.1 % vs. 14.7 %). C4, with a

634   prominent peak at Ex = 230 nm and Em = 308 nm and a second peak at Ex = 275 nm

635   and Em = 305 nm, was characterized as a protein-like component (Yan and Kim, 2017;

636   Wu et al., 2019a; Chen et al., 2020b). C4 was the single largest contributor (42.9 %)

637   during SS particualy during daytime (55.0 %), but became the least during CS (18.0 %).

638   Similarly for MSOC, three HULIS-related fluorophores (C1 ~ C3) and one

639   proteinaceous fluorophore (C4) were separated (Fig. 8b). The spectral signatures

640   between the two series of fluorophores were slightly different, with the MSOC peak

641   excitation and emission wavelengths being a bit larger than those of WSOC, especailly

642   for C2 and C3. Figure S8b shows contributions of the different components to MSOC

643   fluorescene. C1 was much more important in MSOC (26.6 % in SS and 39.2 % in CS)

644   than in WSOC, and became the largest contributor of MSOC during CS; summed C2

645   and C3 contributions (30.7 % in SS and 37.0 % in CS) were on the other hand much

646   less than in WSOC; C4 remained to be the largest (42.6 %) similar to that in WSOC

647   during SS. The increased contributions of the protein-like fluorophore (C4) during SS

648   in both WSOC and MSOC were likely due to its major origin of biological activities,

649   which can be enhanced by the relatively high temperatures during SS (Fan et al., 2020);

650   this is likely the reason that C4 contributions during daytime were higher than those

651   during nightime in both SS and CS. Furthermore, some studies (Barsotti et al., 2016;

652 Chen et al., 2021; Chen et al., 2020b; Cao et al., 2021; Deng et al., 2022) also point out

653 that C4 not only contains proteinaceous species from biological activities but also

654 certain PAHs or phenolic substances from fossil fuel and/or biomass burning, especially

655 in urban aerosols. Probably, the proteinaceous species dominated the fluorescence

656 during SS for both WSOC and MSOC, while during CS PAHs and phenolic compounds

657 became more important and they might prefer to dissolve in methanol therefore lead to

658 its higher contribution in MSOC than in WSOC (23.8 % vs. 18.0 %). Different

659 solubilities of HULIS components in water and methanol may partially lead to their

660 different contributions in WSOC and MSOC.

661

662 **3.3 Molecular composition of organics**

663 **3.3.1 Overview of identified molecules**

664 We classified the identified molecular formulas of organics (here MSOA) via

665 UPLC-QTOF-MS analysis into 8 categories, namely CH, CHO, CHN, CHS, CHON,

666 CHOS, CHNS, and CHONS. Overall, the negative (ESI$^-$) and positive (ESI$^+$) ion modes

667 identified 466 ~ 865 and 644 ~ 1065 formulas, respectively (details in Table S1).

668 Figures S9 and S10 shows the number and signal fractions (relative abundances of

669 signal intensities) of different classes of compounds, respectively.

670 Under ESI$^+$ mode, CHON compounds were the most abundant species in term of

671 the number fraction – nearly half during SS (daytime 50.5 % and nighttime 46.9 %),

672 and over half during CS (daytime 54.1 % and nighttime 55.1 %), and the abundance of

673 its signal was even more prevailing – over half in all cases and up to 67.7 % during SS

674 daytime; the second abundant species were CHO compounds, occupying 23.0 ~ 30.6 %

675 of the total number of molecules and 15.4 ~ 21.9 % of the total signal intensity; CHONS

676 and CHN species were the other two relatively abundant classes – together occupying

677 ~ 20 % (number fraction) and ~ 10 ~ 24 % (signal fraction) of total identified

678 compounds; contributions of other four classes of compounds were very minor, in terms

679 of both number and signal intensity. Relatively, under ESI$^-$ mode, CHO compounds

680 marginally prevailed over CHON compounds in number (36.2 ~ 44.4 % vs. 32.6 ~

681 38.0 %), but during CS their signal fractions were still lower (33.3 ~ 35.1 % vs. 39.3 ~

682 46.5 %). More enrichment of CHO compounds in ESI⁻ than in ESI⁺ is consistent with

683 a previous work (Lin et al., 2012) as these compounds most likely contain carboxyl

684 groups and are easily deprotonated in ESI⁻ mode. Number fractions of CHONS

685 compounds in ESI⁻ mode were ~5 ~ 10% more than those in ESI⁺ mode, while the most

686 contrasting difference was that CHN compounds were rarely detected in ESI⁺ mode,

687 and instead CHOS compounds that were negligible in ESI⁻ mode could be effectively

688 detected in ESI⁺ mode (3.9 ~ 4.8 % in number) and their signal fractions were more

689 significant (6.4 ~ 17.4 %).

690 **3.3.2 CHO compounds**

691 For the detected CHO compounds, we plotted them in the van Krevelen (VK)

692 diagrams according to their H/C and O/C ratios in Fig. 9. Most molecules had the O/C

693 ratios < 0.5, but a broad distribution of H/C ratios (0.5 ~ 2.0). Molecules with high H/C

694 ratios (≥ 1.5) and low O/C ratios (≤ 0.5) (Region A) were typically associated with

695 aliphatic compounds, while those with low H/C ratios (≤ 1.0) and low O/C ratios (≤ 0.5)

696 (Region B) are usually assigned to oxygenated aromatics (Kourtchev et al., 2014). We

697 further calculated the Xc values of all CHO compounds to investigate their molecular

698 structures in Fig. 9. Clearly, saturated aliphatic CHO compounds (Xc < 2.5) were most

699 abundant (323 out of 418 in ESI⁺ mode, and 315 out of 481 in ESI⁻ mode) and mainly

700 distributed in Region A. Appreciate number of unsaturated compounds particularly

701 those with benzene ring or naphthalene ring structures (2.5 < Xc < 2.8), distributed

702 across from H/C of 0.5 to 1.75 but with O/C < 0.5 in ESI⁻ mode and from H/C of 0.1 to

703 1.75 but with a few in the side of O/C > 0.5.

704 The oxygenation state (OS$_c$) (Kroll et al., 2011) (defined as 2*O/C - H/C), is

705 another metric to assess the ageing/oxidation degree of a compound. Figure 10

706 illustrates the dependence of OS$_c$ on carbon number for all CHO compounds. The

707 molecules had a broad coverage of OS$_c$ (-2 to +2) and carbon number (up to 50). Kroll

708 et al. (2011) grouped the compounds into different origins according to their OS$_c$ and C

709 numbers, including fossil fuel combustion HOA, BBOA, semi-volatile oxygenated OA

710 (SV-OOA, typically less-oxidized) and low-volatility oxygenated OA (LV-OOA,

711 typically more-oxidized), as marked in Fig. 10. Obviously, for both ESI$^-$ and ESI$^+$

712 modes, a large portion of compounds belonged to HOA and BBOA. In ESI$^+$ mode, a

713 significant portion of molecules located in the BBOA region, while in ESI$^-$ mode, more

714 molecules tended to be found in the HOA region, and even more molecules located

715 within HOA regime during CS than during SS (Figs. S11 and S12), indicating large

716 influences from anthropogenic emissions. Besides, the number of nighttime LV-OOA

717 molecules was more than that of daytime particular during CS, acting as a supporting

718 evidence of aqueous/heterogeneous reactions.

719 **3.3.3 CHON and CHN compounds**

720 We mapped the detected CHON compounds colored by Xc in the VK diagrams

721 shown in Fig. 11. The compounds were sorted into different series according to the

722 functional groups as well. For ESI$^+$ mode (Fig. 11a), the compounds containing a -NO

723 moiety were dominant and a majority of CHON compounds were saturated with Xc <

724 2.5. Among them, $C_6H_{15}NO(CH_2)_n$ might be N,N-diethylethanolamine homologous

725 compounds, and $C_6H_{15}NO_2(CH_2)_n$ might be diisopropanolamine homologous

726 compounds, as both compounds possess lone pair electrons, prone to positive charge

727 (Ge et al., 2011). Unsaturated CHON compounds with $X_C \geq 2.5$ located in the bottom-

728 left corner, such as $C_5H_5NO(CH_2)_n$, $C_7H_7NO(CH_2)_n$, $C_8H_7NO(CH_2)_n$, and

729 $C_9H_7NO(CH_2)_n$, likely homologous compounds of hydroxypyridine, benzamide,

730 4hydroxy-benzene acetonitrile, and hydroxyquinoline, respectively (Ma and Hays,

731 2008; Wang et al., 2020). In ESI$^-$ mode, the compounds scattered wider than those in

732 ESI$^+$ mode in the VK plot (Fig. 11b), and the majority of them contained one or two

733 nitrogen atoms. Over 25 % of the CHON formulas can be classified as monocyclic or

734 polycyclic compounds with Xc $\geq$ 2.5 (even up to 68 % during SS daytime; inferred

735 from Figs. S13 and S14). The identified series of homologous compounds mostly

736 situated in the bottom-left corner and also with Xc $\geq$ 2.5, such as $C_6H_5NO_3(CH_2)_n$,

737 $C_6H_5NO_4(CH_2)_n$, $C_8H_7NO_3(CH_2)_n$, $C_8H_7NO_4(CH_2)_n$, and $C_{10}H_7NO_3(CH_2)_n$, likely

738 nitrophenol, nitrocatechol, nitroacetophenone, nitrophenylacetic acid, and

739 nitronaphthol homologues, respectively (Wang et al., 2018b; Song et al., 2019; Lin et

740 al., 2017; Lin et al., 2015).

741   As stated in Sect. 3.3.1, CHN compounds were only enriched in ESI$^+$ mode. The

742 scatter plot of H/C versus N/C of these compounds is depicted in Fig. 12 (results of

743 different periods are shown in Fig. S15). Similarly, they are colored by Xc and sorted

744 into a number of different series. Most of these compounds were amines with one or

745 two N atoms. The series of aliphatic amines and other monocyclic species with $X_C <$

746 2.71 mostly located in upper part of the plot, including $C_6H_{15}N(CH_2)_n$, $C_5H_{11}N(CH_2)_n$

747 and $C_6H_{12}N(CH_2)_n$, $C_4H_6N_2(CH_2)_n$, $C_5H_6N_2(CH_2)_n$, $C_7H_6N_2(CH_2)_n$, and $C_{11}H_{17}N(CH_2)_n$.

748 Note the presence of 2 N-heterocyclic species was a sign of presence of BBOA (Wang

749 et al., 2017). The series of $C_{10}H_9N(CH_2)_n$ (1N-PAHs) with $X_C \geq 2.71$ may represent the

750 aminonaphthalene homologues (Ge et al., 2011), likely from initial burning of

751 carbonaceous materials (Mao et al., 2022).

752 **3.3.4 CHOS and CHONS compounds**

753   Among the CHOS formulas (only significant in ESI$^-$ mode), ones with O/S ratios

754 ≥ 4 were classified as organosulfates (OSs), which were the most abundant type (Table

755 4). Its number fractions were particularly high during CS (daytime 54.3 %, nighttime

756 68.6 %), reiterating the importance of aqueous SOA formation during CS. For the

757 CHONS compounds, in ESI$^-$ mode, 5.3 ~ 12.5 % of the formulas had O/(4S+3N) ratios

758 ≥ 1, allowing them to be assigned to –OSO$_3$H and –ONO$_2$ groups, namely nitrooxy-

759 organosulfates (nitrooxy-OSs) (Wang et al., 2018a); while in ESI$^+$ mode, 9.8 ~ 11.8%

760 of total CHONS formulas were apportioned as nitrooxy-OSs (Table 4).

761

762 **3.4 Machine learning assisted identification of key BrC molecules**

763   To enhance the robustness of ML analysis, we first incorporated all detected

764 compounds without assigned molecular formulas of both positive and negative modes

765 (4953 formulas, ESI$^+$: 2863, ESI$^-$: 2090) into the ML model. After ML analysis, a total

766 of 1477 molecules (ESI$^+$: 795; ESI$^-$: 682) were found to have positive values for both

767 IncNPu_val and IncMSE_val. Among them, 1051 molecules (ESI$^+$: 420; ESI$^-$: 450)

768 were assigned corresponding molecular formulas; and furthermore, a total of 149

769 compounds with 0.5<DBE/C<0.9 (ESI$^+$: 52; ESI$^-$: 97) were chosen. By comparing with

770 the database, we finally proposed 31 compounds (ESI$^+$: 18, ESI$^-$: 13) as the key BrC

771 species; details regarding their molecular formulas and proposed structures, etc., are

772 summarized in Table S2. These species are relevant with 4 out of 8 identified types of

773 compounds (CH, CHO, CHN and CHON) (Fig. 13). To the best of our knowledge, 6

774 out of the 31 species (4-methylcoumarin, urocanate, 3-hydroxybenzoic acid, chrysin,

775 2-hydroxypyridine and 4-hydroxyacetophenone) have not been reported before as

776 important BrC species.

777   Two PAHs (acenapthylene and fluoranthene, belonging to CH category) in ESI$^+$

778 mode were identified, consistent with that PAHs are known important BrC (Aurell et

779 al., 2015; Kuang et al., 2021).

780   Twelve CHO compounds (5 in ESI$^+$ mode and 7 in ESI$^-$ mode) were identified. In

781 ESI$^+$ mode, 9-fluorenone and benzanthrone belonging to oxyheterocyclic PAHs (O-

782 PAHs), are known as important BrC chromophores (Kuang et al., 2023); scopoletin is

783 also known as a light-absorbing compound (Zhang, 2018); phthalic anhydride is an

784 oxygen-containing heterocyclic compound. A previous study reports that methanol (the

785 solvent used here) might react with conjugated carbonyl species (such as phthalic

786 anhydride, maleic anhydride, and maleimide) (Chen et al., 2022), thereby affecting the

787 light absorption of relevant BrC species, further studies are needed to verify phthalic

788 anhydride as a key chromophore. In ESI$^-$ mode, a pair of quinone isomers (1-

789 hydroxyanthraquinone and 2-hydroxyanthraquinone) were resolved, in agreement with

790 Kuang et al. (2023), which identified 1-hydroxyanthraquinone as a BrC chromophore

791 in Beijing; 1-hydroxypyrene is a hydroxylated PAHs , also proven as a BrC before

792 (Huang et al., 2022).

793   The identified seven CHN compounds (exclusively in ESI$^+$ mode) included 4 N-

794 heterocyclics, 2 nitro-PAHs, and 1 quinoline compound. It is well known that biomass

795 burning (BB) release a lot of BrC species. As mentioned earlier, CHN compounds are

796 abundant in BB emissions (such as agricultural waste burning and forest fires (Laskin

797 et al., 2009)); small N-containing heterocyclic compounds with one or two aromatic

798 rings, can be effectively produced from thermal decomposition of plants (Ma and Hays,

799 2008), and high temperature pyrolysis of CHN compounds and N-containing plant

800 materials, can result in N-PAHs (Lin et al., 2016). Therefore, identification of the CHN

801 species here as key BrC chromophores are well justified.

802 The remaining confirmed BrC molecules included 10 CHON compounds (4 in

803 ESI$^+$ mode and 6 in ESI$^-$ mode). For ESI$^-$ mode, 3-hydroxyanthranilic acid is an amino

804 phenolic compound $^-$, and the rest five compounds are all nitrophenols, well known as

805 BrC (Li et al., 2020). Another amino phenolic compound, 2-aminophenol was identified

806 in ESI$^+$ mode. Previously, efficient light absorption at 275 nm of 2-aminophenol has

807 been reported, which can be further enhanced in the presence of Fe^{3+} due to formation

808 of oligomers (Al-Abadleh et al., 2022). For acridone in ESI$^+$ mode, earlier studies have

809 shown that acridine exhibits increased light absorbance in the wavelength range of 260

810 $\sim$ 320 nm under irradiation in N$_2$, air, or O$_2$; additionally, a deep yellow layer forms on

811 the surface, indicating the production of light-absorbing products, which was identified

812 as acridone (Negron-Encarnacion and Arce, 2007).

813 For the BrC species identified here, most species contain at least one benzene ring

814 (such as PAHs and NACs) except two compounds (2-hydroxypyridine and urocanate)

815 with other aromatic ring structures. This is reasonable as organic compounds with

816 benzene or other aromatic rings (with conjugated double bonds) are known to be strong

817 light-absorbing. The -OH and -COOH groups on the benzene ring can enhance

818 ultraviolet light absorption at near-UV wavelengths (Jacobson, 1999); The -NO$_2$ group

819 can further increase light absorbance at longer wavelengths (Jacobson, 1999). Our

820 identified BrC list does include compounds with such functional groups. Note some

821 nitrogen-containing heterocyclic compounds, are usually secondary products of

822 aqueous reactions between carbonyl compounds (such as glyoxal and methylglyoxal)

823 and amines or ammonium (Powelson et al., 2014); thus identification of them here as

824 key BrC species is also a supporting evidence of the occurrence of aqueous reactions.

825

4 Conclusions

This work performed a comprehensive investigation on the chemical and optical properties of BrC in ambient $PM_{2.5}$ samples. Regarding the chemical properties, it was found that methanol was able to extract more OC than water (~82.0% vs. 49.5 ~ 61.3% of total OC). The WSOA was composed of two primary factors relevant with fossil fuel combustion (HOA) and biomass burning (BBOA), and two SOA factors (a less oxidized OOA1 and a highly oxygenated OOA2). During CS, OOA2 was abundant (38.6 ~ 43.5 %) while during SS OOA1 was abundant (47.5 ~ 49.8 %); HOA was also an important contributor in both seasons (29.9 ~ 41.7%) but BBOA contribution was relatively minor (7.2 ~ 13.0 %). Further analyses reveal that OOA1 was mainly associated with photochemical reactions while OOA2 was strongly linked with aqueous/heterogeneous reactions.

Regarding the optical properties, our observation shows that $Abs_{365, MSOC}$ was typically larger than $Abs_{365, WSOC}$, but though $MAE_{365, MSOC}$ was still larger than $MAE_{365, WSOC}$ during SS, it became smaller than the $MAE_{365, WSOC}$ during CS, likely owing to that the air mass trajectories during CS significantly intercepted sea/coastal air. The light absorbing abilities of both WSOC and MSOC were weak, but our observations suggest that aqueous oxidation can lead to significant photo-enhancement, therefore the light absorption of WSOA was dominated by OOA2 (50.7 ~ 63.0 %) during CS; while photochemical oxidation could cause a photo-bleaching effect and therefore the contribution of OOA1 to WSOA absorbance was small (15.0 ~ 16.2 %), and HOA contribution was prevailing during SS (55.6 ~ 63.7 %). PARAFAC analysis on the fluorescent spectra of WSOC and MSOC both resolved four key components, including three HULIS component and one protein-like component. HIX, BIX and FI indices also suggest that both WSOC and MSOC originated from a mix of terrestrial and microbial/biogenic sources.

The molecular analysis determined 644 ~ 1065 molecules in ESI^+ mode and 466 ~ 865 molecules in ESI^- mode. Overall, CHON compounds were the most abundant type especially in ESI^+ mode, while CHO compounds slightly exceeded CHON compounds

in number but were still lower in signal intensity. CHN compounds was the third important class and only detectable in ESI$^+$ mode. The VK diagrams further demonstrate the different aromaticity equivalent (Xc) values and evolution pathways of the different classes of compounds. In addition, significant presence of organosulfates and nitroxy-organosulfates in CS samples especially during nighttime re-affirm the importance of aqueous-phase oxidation during CS. Finally, based on the molecular characterization and light absorption measurement results, we applied the ML RF algorithm to identify the key BrC molecules, and we successfully identified 31 key species, including mainly the PAHs, oxyheterocyclic PAHs (O-PAHs), quinones and N-containing compounds; some of them are newly identified.

Of course, our study has some limitations. One limitation is that no source apportionment was conducted on MSOA due to technical difficulties, therefore a full closure between emission sources and optical properties of total OA is incomplete; development of proper method should be the subject of our future work. Moreover, our findings here expand the understanding on chemical (both bulk and molecular level) and optical properties (both light absorption and fluorescence) of BrC, and are valuable to evaluate its impact on air quality and radiation balance; the identified list of key BrC molecules can be a useful reference for future studies. However, our practice with ML approach here serves as only a case study and a valuable attempt, more studies likely with more advanced ML algorithms are needed to identify more BrC species, and to achieve a quantitative closure between the BrC molecules and its total light absorption.

Code availability. The software code to analyze the SP-AMS data is publicly available at: https://cires1.colorado.edu/jimenez-group/ToFAMSResources/ToFSoftware/index.html. The software code to analyze the UPLC-QTOF-MS data is publicly available at: https://systemsomicslab.github.io/compms/msdial/main.html. The software code using SERRF to normalize UPLC-QTOF-MS data is available at: https://slfan.shinyapps.io/ShinySERRF/

884

Data availability. The data in this study are available from the authors upon request

(caxinra@163.com).

887

Supplement. The supplement related to this article is available online at: XXX

889

Author contributions. YH, XL and DDH conducted the experiments. YH, XL, RL,

BZ, YZ and XG performed the data analysis. YH and XG wrote the paper. All authors

reviewed the paper and provide useful suggestions.

893

Competing interests. The contact author has declared that neither they nor their co-

authors have any competing interests.

896

Disclaimer. Publisher's note: Copernicus Publications remains neutral with regard to

jurisdictional claims in published maps and institutional affiliations.

899

Acknowledgements. We sincerely thank the logistic help from the Center for

Experimental Atmospheric Science and Environmental Meteorology of Nanjing

University of Information Science and Technology (NUIST) during sampling.

903

Financial support. This work has been supported by the National Natural Science

Foundation of China (grant nos. 22361162668 and 42021004).

906

Review statement. This paper was edited by XXX, and XXX.

908

References

Aiken, A. C., DeCarlo, P. F., Kroll, J. H., Worsnop, D. R., Huffman, J. A., Docherty, K. h. S., Ulbrich, I. M., Mohr, C., Kimmel, J. l. R., Sueper, D., Sun, Y. l., Zhang, Q., Trimborn, A., Northway, M., Ziemann, P. J., Canagaratna, M. a. R., Onasch, T. B., Alfarra, M. R., Prevot, A. S. H., Dommen, J., Duplissy, J., Metzger, A., Baltensperger, U., and Jimenez, J. L.: O/C and OM/OC ratios of primary, secondary, and ambient organic aerosols with high-resolution time-of-flight aerosol mass

spectrometry, Environ. Sci. Technol., 42, 4478-4485, https://doi.org/10.1021/es703009q, 2008.

Aiona, P. K., Lee, H. J., Leslie, R., Lin, P., Laskin, A., Laskin, J., and Nizkorodov, S. A.: Photochemistry of products of the aqueous reaction of methylglyoxal with ammonium sulfate, ACS Earth Space Chem., 1, 522-532, https://doi.org/10.1021/acsearthspacechem.7b00075, 2017.

Al-Abadleh, H. A., Motaghedi, F., Mohammed, W., Rana, M. S., Malek, K. A., Rastogi, D., Asa-Awuku, A. A., and Guzman, M. I.: Reactivity of aminophenols in forming nitrogen-containing brown carbon from iron-catalyzed reactions, Commun. Chem., 5, 112, https://doi.org/10.1038/s42004-022-00732-1, 2022.

Andreae, M. O. and Gelencsér, A.: Black carbon or brown carbon? The nature of light-absorbing carbonaceous aerosols, Atmos. Chem. Phys., 6, 3131-3148, https://doi.org/10.5194/acp-6-3131-2006, 2006.

Aurell, J., Gullett, B. K., and Tabor, D.: Emissions from southeastern U.S. Grasslands and pine savannas: Comparison of aerial and ground field measurements with laboratory burns, Atmos. Environ., 111, 170-178, https://doi.org/10.1016/j.atmosenv.2015.03.001, 2015.

Bae, E., Yeo, I. J., Jeong, B., Shin, Y., Shin, K. H., and Kim, S.: Study of double bond equivalents and the numbers of carbon and oxygen atom distribution of dissolved organic matter with negative-mode FT-ICR MS, Analytical Chemistry, 83, 4193-4199, https://doi.org/10.1021/ac200464q, 2011.

Bai, D. P., Wang, H. L., Tan, Y., Yin, Y., Wu, Z. J., Guo, S., Shen, L. J., Zhu, B., Wang, J. H., and Kong, X. C.: Optical properties of aerosols and chemical composition apportionment under different pollution levels in Wuhan during January 2018, https://doi.org/10.3390/atmos11010017, 2020.

Barsotti, F., Ghigo, G., and Vione, D.: Computational assessment of the fluorescence emission of phenol oligomers: A possible insight into the fluorescence properties of humic-like substances (HULIS), J. Photochem. Photobiol., A, 315, 87-93, https://doi.org/10.1016/j.jphotochem.2015.09.012, 2016.

Bhowmik, H. S., Tripathi, S. N., Shukla, A. K., Lalchandani, V., Murari, V., Devaprasad, M., Shivam, A., Bhushan, R., Prévôt, A. S. H., and Rastogi, N.: Contribution of fossil and biomass-derived secondary organic carbon to winter water-soluble organic aerosols in Delhi, India, Sci. Total Environ., 912, 168655, https://doi.org/10.1016/j.scitotenv.2023.168655, 2024.

Birdwell, J. E. and Engel, A. S.: Characterization of dissolved organic matter in cave and spring waters using UV–Vis absorbance and fluorescence spectroscopy, Org. Geochem., 41, 270-280, https://doi.org/10.1016/j.orggeochem.2009.11.002, 2010.

Bond, T. C. and Bergstrom, R. W.: Light absorption by carbonaceous particles: an investigative review, Aerosol Sci. Technol., 40, 27-67, https://doi.org/10.1080/02786820500421521, 2006.

Bones, D. L., Henricksen, D. K., Mang, S. A., Gonsior, M., Bateman, A. P., Nguyen, T. B., Cooper, W. J., and Nizkorodov, S. A.: Appearance of strong absorbers and fluorophores in limonene-O3 secondary organic aerosol due to NH4+-mediated chemical aging over long time scales, J. Geophys. Res.: Atmos., 115, https://doi.org/10.1029/2009JD012864, 2010.

Bozzetti, C., El Haddad, I., Salameh, D., Daellenbach, K. R., Fermo, P., Gonzalez, R., Minguillón, M. C., Iinuma, Y., Poulain, L., Elser, M., Müller, E., Slowik, J. G., Jaffrezo, J. L., Baltensperger, U., Marchand, N., and Prévôt, A. S. H.: Organic aerosol source apportionment by offline-AMS over a full year in Marseille, Atmos. Chem. Phys., 17, 8247-8268, https://doi.org/10.5194/acp-17-8247-2017, 2017.

Brown, H., Wang, H. L., Flanner, M., Liu, X. H., Singh, B., Zhang, R. D., Yang, Y., and Wu, M. X.: Brown Carbon Fuel and Emission Source Attributions to Global Snow Darkening Effect, J ADV MODEL EARTH SY, 14, https://doi.org/10.1029/2021ms002768, 2022.

Budisulistiorini, S. H., Riva, M., Williams, M., Chen, J., Itoh, M., Surratt, J. D., and Kuwata, M.: Light-absorbing brown carbon aerosol constituents from combustion of indonesian peat and biomass, Environ. Sci. Technol., 51, 4415-4423, https://doi.org/10.1021/acs.est.7b00397, 2017.

Cain, J., Laskin, A., Kholghy, M. R., Thomson, M. J., and Wang, H.: Molecular characterization of organic content of soot along the centerline of a coflow diffusion flame, Phys. Chem. Chem. Phys., 16, 25862-25875, https://doi.org/10.1039/C4CP03330B, 2014.

Canagaratna, M. R., Jayne, J. T., Ghertner, D. A., Herndon, S., Shi, Q., Jimenez, J. L., Silva, P. J., Williams, P., Lanni, T., Drewnick, F., Demerjian, K. L., Kolb, C. E., and Worsnop, D. R.: Chase studies of particulate emissions from in-use New York City vehicles, Aerosol Sci. Technol., 38, 555-573, https://doi.org/10.1080/02786820490465504, 2004.

Canagaratna, M. R., Jimenez, J. L., Kroll, J. H., Chen, Q., Kessler, S. H., Massoli, P., Hildebrandt Ruiz, L., Fortner, E., Williams, L. R., Wilson, K. R., Surratt, J. D., Donahue, N. M., Jayne, J. T., and Worsnop, D. R.: Elemental ratio measurements of organic compounds using aerosol mass spectrometry: characterization, improved calibration, and implications, Atmos. Chem. Phys., 15, 253-272, https://doi.org/10.5194/acp-15-253-2015, 2015.

Cao, T., Li, M. J., Zou, C. L., Fan, X. J., Song, J. Z., Jia, W. L., Yu, C. L., Yu, Z. Q., and Peng, P. A.: Chemical composition, optical properties, and oxidative potential of water- and methanol-soluble organic compounds emitted from the combustion of biomass materials and coal, Atmos. Chem. Phys., 21, 13187-13205, https://doi.org/10.5194/acp-21-13187-2021, 2021.

Cavalli, F., Facchini, M. C., Decesari, S., Mircea, M., Emblico, L., Fuzzi, S., Ceburnis, D., Yoon, Y. J., O'Dowd, C. D., Putaud, J. P., and Dell'Acqua, A.: Advances in characterization of size-resolved organic matter in marine aerosol over the North Atlantic, J. Geophys. Res.: Atmos., 109, https://doi.org/10.1029/2004JD005137, 2004.

Chakrabarty, R. K., Moosmüller, H., Chen, L. W. A., Lewis, K., Arnott, W. P., Mazzoleni, C., Dubey, M. K., Wold, C. E., Hao, W. M., and Kreidenweis, S. M.: Brown carbon in tar balls from smoldering biomass combustion, Atmos. Chem. Phys., 10, 6363-6370, https://doi.org/10.5194/acp-10-6363-2010, 2010.

Chakrabarty, R. K., Shetty, N. J., Thind, A. S., Beeler, P., Sumlin, B. J., Zhang, C., Liu, P., Idrobo, J. C., Adachi, K., Wagner, N. L., Schwarz, J. P., Ahern, A., Sedlacek, A. J., 3rd, Lambe, A., Daube, C., Lyu, M., Liu, C., Herndon, S., Onasch, T. B., and Mishra, R.: Shortwave absorption by wildfire smoke dominated by dark brown carbon, Nat Geosci, 16, 683-688, https://doi.org/10.1038/s41561-023-01237-9, 2023.

Chen, K. P., Raeofy, N., Lum, M., Mayorga, R., Woods, M., Bahreini, R., Zhang, H. F., and Lin, Y. H.: Solvent effects on chemical composition and optical properties of extracted secondary brown carbon constituents, Aerosol Sci. Technol., 56, 917-930, https://doi.org/10.1080/02786826.2022.2100734, 2022.

Chen, Q. C., Hua, X. Y., Li, J. W., Chang, T., and Wang, Y. Q.: Diurnal evolutions and sources of water-soluble chromophoric aerosols over Xi'an during haze event, in Northwest China, Sci. Total Environ., 786, 147412, https://doi.org/10.1016/j.scitotenv.2021.147412, 2021.

Chen, Q. C., Li, J. W., Hua, X. Y., Jiang, X. T., Mu, Z., Wang, M. M., Wang, J., Shan, M., Yang, X. D., Fan, X. J., Song, J. Z., Wang, Y. Q., Guan, D. J., and Du, L.: Identification of species

and sources of atmospheric chromophores by fluorescence excitation-emission matrix with parallel factor analysis, Sci. Total Environ., 718, 137322, https://doi.org/10.1016/j.scitotenv.2020.137322, 2020a.

Chen, Q. C., Miyazaki, Y., Kawamura, K., Matsumoto, K., Coburn, S., Volkamer, R., Iwamoto, Y., Kagami, S., Deng, Y. G., Ogawa, S. H., Ramasamy, S., Kato, S., Ida, A., Kajii, Y., and Mochida, M.: Characterization of chromophoric water-soluble organic matter in urban, forest, and marine aerosols by HR-ToF-AMS analysis and excitation–emission matrix spectroscopy, Environ. Sci. Technol., 50, 10351-10360, https://doi.org/10.1021/acs.est.6b01643, 2016.

Chen, Y. and Bond, T. C.: Light absorption by organic carbon from wood combustion, Atmos. Chem. Phys., 10, 1773-1787, https://doi.org/10.5194/acp-10-1773-2010, 2010.

Chen, Y. F., Ge, X. L., Chen, H., Xie, X. C., Chen, Y. T., Wang, J. F., Ye, Z. L., Bao, M. Y., Zhang, Y. L., and Chen, M. D.: Seasonal light absorption properties of water-soluble brown carbon in atmospheric fine particles in Nanjing, China, Atmos. Environ., 187, 230-240, https://doi.org/10.1016/j.atmosenv.2018.06.002, 2018.

Chen, Y. F., Xie, X. C., Shi, Z., Li, Y. L., Gai, X. Y., Wang, J. F., Li, H. W., Wu, Y., Zhao, X. Y., Chen, M. D., and Ge, X. L.: Brown carbon in atmospheric fine particles in Yangzhou, China: Light absorption properties and source apportionment, Atmos. Res., 244, 105028, https://doi.org/10.1016/j.atmosres.2020.105028, 2020b.

Cheng, Y., He, K. B., Du, Z. Y., Engling, G., Liu, J. M., Ma, Y. L., Zheng, M., and Weber, R. J.: The characteristics of brown carbon aerosol during winter in Beijing, Atmos. Environ., 127, 355-364, https://doi.org/10.1016/j.atmosenv.2015.12.035, 2016.

Coble, P. G.: Characterization of marine and terrestrial DOM in seawater using excitation-emission matrix spectroscopy, Mar. Chem., 51, 325-346, https://doi.org/10.1016/0304-4203(95)00062-3, 1996.

Daellenbach, K. R., Stefenelli, G., Bozzetti, C., Vlachou, A., Fermo, P., Gonzalez, R., Piazzalunga, A., Colombi, C., Canonaco, F., Hueglin, C., Kasper-Giebl, A., Jaffrezo, J. L., Bianchi, F., Slowik, J. G., Baltensperger, U., El-Haddad, I., and Prévôt, A. S. H.: Long-term chemical analysis and organic aerosol source apportionment at nine sites in central Europe: source identification and uncertainty assessment, Atmos. Chem. Phys., 17, 13265-13282, https://doi.org/10.5194/acp-17-13265-2017, 2017.

DeLessio, M. A., Tsigaridis, K., Bauer, S. E., Chowdhary, J., and Schuster, G. L.: Modeling atmospheric brown carbon in the GISS ModelE Earth system model, Atmos. Chem. Phys., 24, 6275-6304, https://doi.org/10.5194/acp-24-6275-2024, 2024.

Deng, J. J., Ma, H., Wang, X. F., Zhong, S. J., Zhang, Z. M., Zhu, J. L., Fan, Y. B., Hu, W., Wu, L. B., Li, X. D., Ren, L. J., Pavuluri, C. M., Pan, X. L., Sun, Y. L., Wang, Z. F., Kawamura, K., and Fu, P. Q.: Measurement report: Optical properties and sources of water-soluble brown carbon in Tianjin, North China – insights from organic molecular compositions, Atmos. Chem. Phys., 22, 6449-6470, https://doi.org/10.5194/acp-22-6449-2022, 2022.

Dey, S., Mukherjee, A., Polana, A. J., Rana, A., Mao, J. Y., Jia, S. G., Yadav, A. K., Khillare, P. S., and Sarkar, S.: Brown carbon aerosols in the Indo-Gangetic Plain outflow: insights from excitation emission matrix (EEM) fluorescence spectroscopy, Environ. Sci.: Processes Impacts, 23, 745-755, https://doi.org/10.1039/D1EM00050K, 2021.

Dong, W. M., Wan, J. M., Tokunaga, T. K., Gilbert, B., and Williams, K. H.: Transport and humification of dissolved organic matter within a semi-arid floodplain, J. Environ. Sci, 57, 24-32,

1047 https://doi.org/10.1016/j.jes.2016.12.011, 2017.

1048 Dührkop, K., Fleischauer, M., Ludwig, M., Aksenov, A. r. A., Melnik, A. V., Meusel, M.,
1049 Dorrestein, P. r. C., Rousu, J., and Böcker, S.: SIRIUS 4: a rapid tool for turning tandem mass spectra
1050 into metabolite structure information, Nat. Methods, 16, 299-302, https://doi.org/10.1038/s41592-
1051 019-0344-8, 2019.

1052 Fan, X. J., Wei, S. Y., Zhu, M. B., Song, J. Z., and Peng, P. A.: Comprehensive characterization
1053 of humic-like substances in smoke PM2.5 emitted from the combustion of biomass materials and
1054 fossil fuels, Atmos. Chem. Phys., 16, 13321-13340, https://doi.org/10.5194/acp-16-13321-2016,
1055 2016.

1056 Fan, X. J., Yu, X. F., Wang, Y., Xiao, X., Li, F. Y., Xie, Y., Wei, S. Y., Song, J. Z., and Peng, P.
1057 A.: The aging behaviors of chromophoric biomass burning brown carbon during dark aqueous
1058 hydroxyl radical oxidation processes in laboratory studies, Atmos. Environ., 205, 9-18,
1059 https://doi.org/10.1016/j.atmosenv.2019.02.039, 2019.

1060 Fan, Y., Liu, C. Q., Li, L., Ren, L., Ren, H., Zhang, Z., Li, Q., Wang, S., Hu, W., Deng, J., Wu,
1061 L., Zhong, S., Zhao, Y., Pavuluri, C. M., Li, X., Pan, X., Sun, Y., Wang, Z., Kawamura, K., Shi, Z.,
1062 and Fu, P.: Large contributions of biogenic and anthropogenic sources to fine organic aerosols in
1063 Tianjin, North China, Atmos. Chem. Phys., 20, 117-137, https://doi.org/10.5194/acp-20-117-2020,
1064 2020.

1065 Fasola, S., Maio, S., Baldacci, S., La Grutta, S., Ferrante, G., Forastiere, F., Stafoggia, M.,
1066 Gariazzo, C., and Viegi, G.: Effects of particulate matter on the incidence of respiratory diseases in
1067 the pisan longitudinal study, Int. J. Environ. Res. Public Health, 17,
1068 https://doi.org/10.3390/ijerph17072540, 2020.

1069 Feng, Y., Ramanathan, V., and Kotamarthi, V. R.: Brown carbon: a significant atmospheric
1070 absorber of solar radiation?, Atmos. Chem. Phys., 13, 8607-8621, https://doi.org/10.5194/acp-13-
1071 8607-2013, 2013.

1072 Fleming, L. T., Lin, P., Roberts, J. M., Selimovic, V., Yokelson, R., Laskin, J., Laskin, A., and
1073 Nizkorodov, S. A.: Molecular composition and photochemical lifetimes of brown carbon
1074 chromophores in biomass burning organic aerosol, Atmos. Chem. Phys., 20, 1105-1129,
1075 https://doi.org/10.5194/acp-20-1105-2020, 2020.

1076 Fu, P. Q., Kawamura, K., Chen, J., Qin, M. Y., Ren, L. J., Sun, Y. L., Wang, Z. F., Barrie, L.
1077 A., Tachibana, E., Ding, A. J., and Yamashita, Y.: Fluorescent water-soluble organic aerosols in the
1078 High Arctic atmosphere, Sci. Rep., 5, 9845, https://doi.org/10.1038/srep09845, 2015.

1079 Ge, X. L., Wexler, A. S., and Clegg, S. L.: Atmospheric amines – part I. a review, Atmos.
1080 Environ., 45, 524-546, https://doi.org/10.1016/j.atmosenv.2010.10.012, 2011.

1081 Ge, X. L., Sun, Y. L., Trousdell, J., Chen, M. D., and Zhang, Q.: Enhancing characterization
1082 of organic nitrogen components in aerosols and droplets using high-resolution aerosol mass
1083 spectrometry, Atmos. Meas. Tech., 17, 423-439, https://doi.org/10.5194/amt-17-423-2024, 2024.

1084 Ge, X. L., Li, L., Chen, Y. F., Chen, H., Wu, D., Wang, J. F., Xie, X. C., Ge, S., Ye, Z. L., Xu,
1085 J. Z., and Chen, M. D.: Aerosol characteristics and sources in Yangzhou, China resolved by offline
1086 aerosol mass spectrometry and other techniques, Environ. Pollut., 225, 74-85,
1087 https://doi.org/10.1016/j.envpol.2017.03.044, 2017.

1088 Gilardoni, S., Massoli, P., Paglione, M., Giulianelli, L., Carbone, C., Rinaldi, M., Decesari, S.,
1089 Sandrini, S., Costabile, F., Gobbi, G. P., Pietrogrande, M. C., Visentin, M., Scotto, F., Fuzzi, S., and
1090 Facchini, M. C.: Direct observation of aqueous secondary organic aerosol from biomass-burning

emissions, Proc. Natl. Acad. Sci. U. S. A., 113, 10013-10018, https://doi.org/10.1073/pnas.1602212113, 2016.

González, C., Mira-M., J., and Juárez, I.: Important variable assessment and electricity price forecasting based on regression tree models: classification and regression trees, Bagging and Random Forests, IET Gener. Transm. Dis., 9, 1120-1128, https://doi.org/10.1049/iet-gtd.2014.0655, 2015.

Gu, C. J., Cui, S. J., Ge, X. L., Wang, Z. Y., Chen, M. J., Qian, Z. H., Liu, Z. Y., Wang, X. F., and Zhang, Y. J.: Chemical composition, sources and optical properties of nitrated aromatic compounds in fine particulate matter during winter foggy days in Nanjing, China, Environ. Res., 212, 113255, https://doi.org/10.1016/j.envres.2022.113255, 2022.

Hawkins, L. N., Lemire, A. N., Galloway, M. M., Corrigan, A. L., Turley, J. J., Espelien, B. M., and De H., D. O.: Maillard chemistry in clouds and aqueous aerosol as a source of atmospheric humic-like substances, Environ. Sci. Technol., 50, 7443-7452, https://doi.org/10.1021/acs.est.6b00909, 2016.

Hecobian, A., Zhang, X., Zheng, M., Frank, N., Edgerton, E. S., and Weber, R. J.: Water-soluble organic aerosol material and the light-absorption characteristics of aqueous extracts measured over the southeastern united states, Atmos. Chem. Phys., 10, 5965-5977, https://doi.org/10.5194/acp-10-5965-2010, 2010.

Hu, J. L., Wang, P., Ying, Q., Zhang, H. L., Chen, J. J., Ge, X. L., Li, X. H., Jiang, J. K., Wang, S. X., Zhang, J., Zhao, Y., and Zhang, Y. Y.: Modeling biogenic and anthropogenic secondary organic aerosol in China, Atmos. Chem. Phys., 17, 77-92, https://doi.org/10.5194/acp-17-77-2017, 2017.

Hu, R. L., Xu, Q. C., Wang, S. X., Hua, Y., Bhattarai, N., Jiang, J K., Song, Y., Daellenbach, K. R., Qi, L., Prevot, A. S. H., and Hao, J. M.: Chemical characteristics and sources of water-soluble organic aerosol in southwest suburb of Beijing, J. Environ. Sci., 95, 99-110, https://doi.org/10.1016/j.jes.2020.04.004, 2020.

Huang, L. B., Liu, T. S., and Grassian, V. i. H.: Radical-Initiated formation of aromatic organosulfates and sulfonates in the aqueous phase, Environ. Sci. Technol., 54, 11857-11864, https://doi.org/10.1021/acs.est.0c05644, 2020.

Huang, R. J., Yang, L., Shen, J. C., Yuan, W., Gong, Y. Q., Ni, H. Y., Duan, J., Yan, J., Huang, H. B., You, Q. H., and Li, Y., J.: Chromophoric fingerprinting of brown carbon from residential biomass burning, Environ. Sci. Technol. Lett., 9, 102-111, https://doi.org/10.1021/acs.estlett.1c00837, 2022.

Huang, R. J., Yang, L., Cao, J. J., Chen, Y., Chen, Q., Li, Y. J., Duan, J., Zhu, C. S., Dai, W. T., Wang, K., Lin, C. S., Ni, H. Y., Corbin, J. C., Wu, Y. F., Zhang, R. J., Tie, X. X., Hoffmann, T., O' Dowd, C., and Dusek, U.: Brown carbon aerosol in urban Xi'an, northwest China: the composition and light absorption properties, Environ. Sci. Technol., 52, 6825-6833, https://doi.org/10.1021/acs.est.8b02386, 2018.

Huguet, A., Vacher, L., Relexans, S., Saubusse, S., Froidefond, J. M., and Parlanti, E.: Properties of fluorescent dissolved organic matter in the Gironde Estuary, Org. Geochem., 40, 706-719, https://doi.org/10.1016/j.orggeochem.2009.03.002, 2009.

Jacobson, M. Z.: Isolating nitrated and aromatic aerosols and nitrated aromatic gases as sources of ultraviolet light absorption, J. Geophys. Res.: Atmos., 104, 3527-3542, https://doi.org/10.1029/1998JD100054, 1999.

1135   Jaoui, M., Corse, E., Kleindienst, T. E., Offenberg, J. H., Lewandowski, M., and Edney, E. O.:
1136   Analysis of secondary organic aerosol compounds from the photooxidation of d-limonene in the
1137   presence of NOX and their detection in ambient PM2.5, Environ. Sci. Technol., 40, 3819-3828,
1138   https://doi.org/10.1021/es052566z, 2006.

1139   Jiang, W. Q., Misovich, M. V., Hettiyadura, A. P. S., Laskin, A., McFall, A. S., Anastasio, C.,
1140   and Zhang, Q.: Photosensitized Reactions of a phenolic carbonyl from wood combustion in the
1141   aqueous phase—chemical evolution and light absorption properties of aqSOA, Environ. Sci.
1142   Technol., 55, 5199-5211, https://doi.org/10.1021/acs.est.0c07581, 2021.

1143   Jiang, X. T., Liu, D. T., Li, Q., Tian, P., Wu, Y. Z., Li, S. Y., Hu, K., Ding, S., Bi, K., Li, R. J.,
1144   Huang, M. Y., Ding, D. P., Chen, Q. C., Kong, S. F., Li, W. J., Pang, Y., and He, D.: Connecting the
1145   light absorption of atmospheric organic aerosols with oxidation state and polarity, Environ. Sci.
1146   Technol., 56, 12873-12885, https://doi.org/10.1021/acs.est.2c02202, 2022.

1147   Jo, D. S., Park, R. J., Lee, S., Kim, S. W., and Zhang, X.: A global simulation of brown carbon:
1148   implications for photochemistry and direct radiative effect, Atmos. Chem. Phys., 16, 3413-3432,
1149   https://doi.org/10.5194/acp-16-3413-2016, 2016.

1150   Kim, H. J., Collier, S., Ge, X. L., Xu, J. Z., Sun, Y. L., Jiang, W. Q., Wang, Y. L., Herckes, P.,
1151   and Zhang, Q.: Chemical processing of water-soluble species and formation of secondary organic
1152   aerosol in fogs, Atmos. Environ., 200, 158-166, https://doi.org/10.1016/j.atmosenv.2018.11.062,
1153   2019.

1154   Kourtchev, I., O'Connor, I. P., Giorio, C., Fuller, S. J., Kristensen, K., Maenhaut, W., Wenger,
1155   J. C., Sodeau, J. R., Glasius, M., and Kalberer, M.: Effects of anthropogenic emissions on the
1156   molecular composition of urban organic aerosols: An ultrahigh resolution mass spectrometry study,
1157   Atmos. Environ., 89, 525-532, https://doi.org/10.1016/j.atmosenv.2014.02.051, 2014.

1158   Kroll, J. H., Donahue, N. M., Jimenez, J. L., Kessler, S. H., Canagaratna, M. R., Wilson, K.
1159   R., Altieri, K. E., Mazzoleni, L. R., Wozniak, A. S., Bluhm, H., Mysak, E. R., Smith, J. D., Kolb, C.
1160   E., and Worsnop, D. R.: Carbon oxidation state as a metric for describing the chemistry of
1161   atmospheric organic aerosol, Nat. Chem., 3, 133-139, https://doi.org/10.1038/nchem.948, 2011.

1162   Kuang, Y., Shang, J., and Chen, Q. C.: Effect of ozone aging on light absorption and
1163   fluorescence of brown carbon in soot particles: The important role of polycyclic aromatic
1164   hydrocarbons, J. Hazard. Mater., 413, 125406, https://doi.org/10.1016/j.jhazmat.2021.125406, 2021.

1165   Kuang, Y., Shang, J., Sheng, M. S., Shi, X. D., Zhu, J. L., and Qiu, X. H.: Molecular
1166   Composition of Beijing PM(2.5) Brown Carbon Revealed by an Untargeted Approach Based on Gas
1167   Chromatography and Time-of-Flight Mass Spectrometry, Environ. Sci. Technol., 57, 909-919,
1168   https://doi.org/10.1021/acs.est.2c05918, 2023.

1169   Kumar, V., Giannoukos, S., Haslett, S. L., Tong, Y., Singh, A., Bertrand, A., Lee, C. P., Wang,
1170   D. S., Bhattu, D., Stefenelli, G., Dave, J. S., Puthussery, J. V., Qi, L., Vats, P., Rai, P., Casotto, R.,
1171   Satish, R., Mishra, S., Pospisilova, V., Mohr, C., Bell, D. M., Ganguly, D., Verma, V., Rastogi, N.,
1172   Baltensperger, U., Tripathi, S. N., Prévôt, A. S. H., and Slowik, J. G.: Highly time-resolved chemical
1173   speciation and source apportionment of organic aerosol components in Delhi, India, using extractive
1174   electrospray ionization mass spectrometry, Atmos. Chem. Phys., 22, 7739-7761,
1175   https://10.5194/acp-22-7739-2022, 2022.

1176   Laskin, A., Laskin, J., and Nizkorodov, S. A.: Chemistry of atmospheric brown carbon, Chem.
1177   Rev., 115, 4335-4382, https://doi.org/10.1021/cr5006167, 2015.

1178   Laskin, A., Smith, J. S., and Laskin, J.: Molecular characterization of nitrogen-containing

organic compounds in biomass burning aerosols using high-resolution mass spectrometry, Environ. Sci. Technol., 43, 3764-3771, https://doi.org/10.1021/es803456n, 2009.

Laskin, A., West, C. P., and Hettiyadura, A. P. S.: Molecular insights into the composition, sources, and aging of atmospheric brown carbon, Chem Soc Rev, 54, 1583-1612, 10.1039/d3cs00609c, 2025.

Lee, H. L., Laskin, A., Laskin, J., and Nizkorodov, S. A.: Excitation–emission spectra and fluorescence quantum yields for fresh and aged biogenic secondary organic aerosols, Environ. Sci. Technol., 47, 5763-5770, https://doi.org/10.1021/es400644c, 2013.

Lei, R. Y., Sha, Y. Y., Meng, H. F., Huang, Y., Ye, J. H., Huang, D. D., Zhang, Y. J., Wu, Y., Li, Y. J., and Ge, X. L.: Aqueous phase photolysis of 4-nitrocatechol: Reaction kinetics, evolutions of chemical composition, light absorption and oxidation potential, Atmos. Environ., 343, 120981, https://doi.org/10.1016/j.atmosenv.2024.120981, 2025.

Li, H., Qin, X. F., Wang, G. C., Xu, J., Wang, Lu, D., Liu, C., Zheng, H., Liu, J. G., Huang, K., and Deng, C. R.: Conjoint impacts of continental outflows and marine sources on brown carbon in the East China sea: Abundances, optical properties, and formation processes, Atmos. Environ., 273, 118959, https://doi.org/10.1016/j.atmosenv.2022.118959, 2022a.

Li, H. W., Cui, L., Huang, Y., Zhang, Y. J., Wang, J. F., Chen, M. D., and Ge, X. L.: Concurrent dominant pathways of multifunctional products formed from nocturnal isoprene oxidation, Chemosphere, 322, 138185, https://doi.org/10.1016/j.chemosphere.2023.138185, 2023.

Li, M., Wang, X. F., Lu, C. Y., Li, R., Zhang, J., Dong, S. W., Yang, L. X., Xue, L., Chen, J. M., and Wang, W. X.: Nitrated phenols and the phenolic precursors in the atmosphere in urban Jinan, China, Sci. Total Environ., 714, 136760, https://doi.org/10.1016/j.scitotenv.2020.136760, 2020.

Li, M. J., Fan, X. J., Zhu, M. B., Zou, C. L., Song, J. Z., Wei, S. Y., Jia, W. L., and Peng, P. A.: Abundance and light absorption properties of brown carbon emitted from residential coal combustion in China, Environ. Sci. Technol., 53, 595-603, https://doi.org/10.1021/acs.est.8b05630, 2019.

Li, S., Chen, C., Yang, G.-l., Fang, J., Sun, Y., Tang, L., Wang, H., Xiang, W., Zhang, H., Croteau, P. L., Jayne, J. T., Liao, H., Ge, X., Favez, O., and Zhang, Y.: Sources and processes of organic aerosol in non-refractory PM1 and PM2.5 during foggy and haze episodes in an urban environment of the Yangtze River Delta, China, Environ. Res., 212, 113557, https://doi.org/10.1016/j.envres.2022.113557, 2022b.

Li, X. D., Tao, Y., Zhu, L. W., Ma, S. S., Luo, S. P., Zhao, Z. Z., Sun, N., Ge, X. L., and Ye, Z. L.: Optical and chemical properties and oxidative potential of aqueous-phase products from OH and 3C∗-initiated photooxidation of eugenol, Atmos. Chem. Phys., 22, 7793-7814, https://doi.org/10.5194/acp-22-7793-2022, 2022c.

Lin, G. X., Penner, J. E., Flanner, M. G., Sillman, S., Xu, L., and Zhou, C.: Radiative forcing of organic aerosol in the atmosphere and on snow: effects of SOA and brown carbon, J. Geophys. Res.: Atmos., 119, 7453-7476, https://doi.org/10.1002/2013JD021186, 2014.

Lin, P., Rincon, A. G., Kalberer, M., and Yu, J. Z.: Elemental composition of HULIS in the pearl river delta region, China: results inferred from positive and negative electrospray high resolution mass spectrometric data, Environ. Sci. Technol., 46, 7454-7462, https://doi.org/10.1021/es300285d, 2012.

Lin, P., Fleming, L. T., Nizkorodov, S. A., Laskin, J., and Laskin, A.: Comprehensive molecular characterization of atmospheric brown carbon by high resolution mass spectrometry with

electrospray and atmospheric pressure photoionization, Anal. Chem., 90, 12493-12502, https://doi.org/10.1021/acs.analchem.8b02177, 2018.

Lin, P., Bluvshtein, N., Rudich, Y., Nizkorodov, S. A., Laskin, J., and Laskin, A.: Molecular chemistry of atmospheric brown carbon inferred from a nationwide biomass burning event, Environ. Sci. Technol., 51, 11561-11570, https://doi.org/10.1021/acs.est.7b02276, 2017.

Lin, P., Liu, J. M., Shilling, J. E., Kathmann, S. M., Laskin, J., and Laskin, A.: Molecular characterization of brown carbon (BrC) chromophores in secondary organic aerosol generated from photo-oxidation of toluene, Phys. Chem. Chem. Phys., 17, 23312-23325, https://doi.org/10.1039/C5CP02563J, 2015.

Lin, P., Aiona, P. K., Li, Y., Shiraiwa, M., Laskin, J., Nizkorodov, S. A., and Laskin, A.: Molecular characterization of brown carbon in ciomass curning aerosol particles, Environ. Sci. Technol., 50, 11815-11824, https://doi.org/10.1021/acs.est.6b03024, 2016.

Liu, Y., Li, H. W., Cui, S. J., Nie, D. Y., Chen, Y. F., and Ge, X. L.: Chemical Characteristics and Sources of Water-Soluble Organic Nitrogen Species in PM2.5 in Nanjing, China, https://doi.org/10.3390/atmos12050574, 2021.

Lobodin, V. V., Marshall, A. G., and Hsu, C. S.: Compositional space boundaries for organic compounds, Analytical Chemistry, 84, 3410-3416, https://doi.org/10.1021/ac300244f, 2012.

Ma, Y. L. and Hays, M. D.: Thermal extraction–two-dimensional gas chromatography–mass spectrometry with heart-cutting for nitrogen heterocyclics in biomass burning aerosols, J. Chromatogr. A, 1200, 228-234, https://doi.org/10.1016/j.chroma.2008.05.078, 2008.

Mao, J. F., Cheng, Y., Bai, Z., Zhang, W., Zhang, L. Y., Chen, H., Wang, L. N., Li, L., and Chen, J. M.: Molecular characterization of nitrogen-containing organic compounds in the winter North China Plain, Sci Total Environ, 838, 156189, https://10.1016/j.scitotenv.2022.156189, 2022.

Matos, J. T. V., Freire, S. M. S. C., Duarte, R. M. B. O., and Duarte, A. C.: Natural organic matter in urban aerosols: comparison between water and alkaline soluble components using excitation–emission matrix fluorescence spectroscopy and multiway data analysis, Atmos. Environ., 102, 1-10, https://doi.org/10.1016/j.atmosenv.2014.11.042, 2015.

McKnight, D. M., Boyer, E. W., Westerhoff, P. K., Doran, P. T., Kulbe, T., and Andersen, D. T.: Spectrofluorometric characterization of dissolved organic matter for indication of precursor organic material and aromaticity, Limnol. Oceanogr., 46, 38-48, https://doi.org/10.4319/lo.2001.46.1.0038, 2001.

McNeill, V. F.: Aqueous organic chemistry in the atmosphere: sources and chemical processing of organic aerosols, Environ. Sci. Technol., 49, 1237-1244, https://doi.org/10.1021/es5043707, 2015.

Murphy, K. R., Stedmon, C. A., Graeber, D., and Bro, R.: Fluorescence spectroscopy and multi-way techniques. PARAFAC, Anal. Methods, 5, https://doi.org/10.1039/c3ay41160e, 2013.

Murphy, K. R., Hambly, A., Singh, S., Henderson, R. K., Baker, A., Stuetz, R., and Khan, S. J.: Organic matter fluorescence in municipal water recycling schemes: toward a unified PARAFAC model, Environ. Sci. Technol., 45, 2909-2916, https://doi.org/10.1021/es103015e, 2011.

Negron-Encarnacion, I. and Arce, R.: Light-induced transformations of aza-aromatic pollutants adsorbed on models of atmospheric particulate matter: Acridine and 9(10-H) acridone, Atmos. Environ., 41, 6771-6783, https://doi.org/10.1016/j.atmosenv.2007.04.062, 2007.

O'Brien, R. E., Ridley, K. J., Canagaratna, M. R., Jayne, J. T., Croteau, P. L., Worsnop, D. R., Budisulistiorini, S. H., Surratt, J. D., Follett, C. L., Repeta, D. J., and Kroll, J. H.: Ultrasonic

nebulization for the elemental analysis of microgram-level samples with offline aerosol mass spectrometry, Atmos. Meas. Tech., 12, 1659-1671, https://doi.org/10.5194/amt-12-1659-2019, 2019.

Onasch, T. B., Trimborn, A., Fortner, E. C., Jayne, J. T., Kok, G. L., Williams, L. R., Davidovits, P., and Worsnop, D. R.: Soot particle aerosol mass spectrometer: development, validation, and initial application, Aerosol Sci. Technol., 46, 804-817, https://doi.org/10.1080/02786826.2012.663948, 2012.

Ou, Y., Nie, D. Y., Chen, H., Ye, Z. L., and Ge, X. L.: Characterization of products from the aqueous-phase photochemical oxidation of benzene-diols, Atmosphere, 12, https://doi.org/10.3390/atmos12050534, 2021.

Petters, S. S., Cui, T. Q., Zhang, Z. F., Gold, A., McNeill, V. F., Surratt, J. D., and Turpin, B. J.: Organosulfates from dark aqueous reactions of isoprene-derived epoxydiols under cloud and fog conditions: kinetics, mechanism, and effect of reaction environment on regioselectivity of sulfate addition, ACS Earth Space Chem., 5, 474-486, https://doi.org/10.1021/acsearthspacechem.0c00293, 2021.

Powelson, M. H., Espelien, B. M., Hawkins, L. N., Galloway, M. M., and De Haan, D. O.: Brown Carbon Formation by Aqueous-Phase Carbonyl Compound Reactions with Amines and Ammonium Sulfate, Environ. Sci. Technol., 48, 985-993, https://doi.org/10.1021/es4038325, 2014.

Qi, L., Chen, M. D., Stefenelli, G., Pospisilova, V., Tong, Y. D., Bertrand, A., Hueglin, C., Ge, X. L., Baltensperger, U., Prévôt, A. S. H., and Slowik, J. G.: Organic aerosol source apportionment in Zurich using an extractive electrospray ionization time-of-flight mass spectrometer (EESI-TOF-MS) – Part 2: biomass burning influences in winter, Atmos. Chem. Phys., 19, 8037-8062, https://doi.org/10.5194/acp-19-8037-2019, 2019.

Qin, J. J., Zhang, L. M., Zhou, X. M., Duan, J. C., Mu, S. T., Xiao, K., Hu, J. N., and Tan, J. H.: Fluorescence fingerprinting properties for exploring water-soluble organic compounds in PM2.5 in an industrial city of northwest China, Atmos. Environ., 184, 203-211, https://doi.org/10.1016/j.atmosenv.2018.04.049, 2018.

Qin, Y. M., Tan, H. B., Li, Y. J., Schurman, M. I., Li, F., Canonaco, F., Prévôt, A. S. H., and Chan, C. K.: Impacts of traffic emissions on atmospheric particulate nitrate and organics at a downwind site on the periphery of Guangzhou, China, Atmos. Chem. Phys., 17, 10245-10258, https://doi.org/10.5194/acp-17-10245-2017, 2017.

Qiu, Y. M., Xie, Q. R., Wang, J. F., Xu, W. Q., Li, L. J., Wang, Q. Q., Zhao, J., Chen, Y. T., Chen, Y. F., Wu, Y. Z., Du, W., Zhou, W., Lee, J., Zhao, C. F., Ge, X. L., Fu, P. Q., Wang, Z., Worsnop, D. R., and Sun, Y. L.: Vertical characterization and source apportionment of water-soluble organic aerosol with high-resolution aerosol mass spectrometry in Beijing, China, ACS Earth Space Chem., 3, 273-284, https://doi.org/10.1021/acsearthspacechem.8b00155, 2019.

Shapiro, E. L., Szprengiel, J., Sareen, N., Jen, C. N., Giordano, M. R., and McNeill, V. F.: Light-absorbing secondary organic material formed by glyoxal in aqueous aerosol mimics, Atmos. Chem. Phys., 9, 2289-2300, https://doi.org/10.5194/acp-9-2289-2009, 2009.

Song, J. Z., Li, M. J., Fan, X. J., Zou, C. L., Zhu, M. B., Jiang, B., Yu, Z. Q., Jia, W. L., Liao, Y. H., and Peng, P. A.: Molecular Characterization of water- and methanol-soluble organic compounds emitted from residential coal combustion using ultrahigh-resolution electrospray ionization fourier transform ion cyclotron resonance mass spectrometry, Environ. Sci. Technol., 53, 13607-13617, https://doi.org/10.1021/acs.est.9b04331, 2019.

Stubbins, A., Lapierre, J. F., Berggren, M., Prairie, Y. T., Dittmar, T., and del Giorgio, P. A.:

What's in an EEM? Molecular Signatures Associated with Dissolved Organic Fluorescence in Boreal Canada, Environ. Sci. Technol., 48, 10598-10606, https://doi.org/10.1021/es502086e, 2014.

Sun, Y. L., Du, W., Fu, P. Q., Wang, Q. Q., Li, J., Ge, X. L., Zhang, Q., Zhu, C. M., Ren, L. J., Xu, W. Q., Zhao, J., Han, T. T., Worsnop, D. R., and Wang, Z.: Primary and secondary aerosols in Beijing in winter: sources, variations and processes, Atmos. Chem. Phys., 16, 8309-8329, https://doi.org/10.5194/acp-16-8309-2016, 2016.

Tang, J., Li, J., Su, T., Han, Y., Mo, Y. Z., Jiang, H. X., Cui, M., Jiang, B., Chen, Y. J., Tang, J. H., Song, J. Z., Peng, P. A., and Zhang, G.: Molecular compositions and optical properties of dissolved brown carbon in biomass burning, coal combustion, and vehicle emission aerosols illuminated by excitation–emission matrix spectroscopy and Fourier transform ion cyclotron resonance mass spectrometry analysis, Atmos. Chem. Phys., 20, 2513-2532, https://doi.org/10.5194/acp-20-2513-2020, 2020.

Tang, J., Li, J., Zhao, S. Z., Zhong, G. C., Mo, Y. Z., Jiang, H. X., Jiang, B., Chen, Y. J., Tang, J. H., Tian, C. G., Zong, Z., Hussain S., J., Song, J. Z., and Zhang, G.: Molecular signatures and formation mechanisms of water-soluble chromophores in particulate matter from Karachi in Pakistan, Sci. Total Environ., 914, 169890, https://doi.org/10.1016/j.scitotenv.2024.169890, 2024.

Tsugawa, H., Cajka, T., Kind, T., Ma, Y., Higgins, B., Ikeda, K., Kanazawa, M., VanderGheynst, J., Fiehn, O., and Arita, M.: MS-DIAL: data-independent MS/MS deconvolution for comprehensive metabolome analysis, Nat. Methods, 12, 523-526, https://doi.org/10.1038/nmeth.3393, 2015.

Ulbrich, I. M., Canagaratna, M. R., Zhang, Q., Worsnop, D. R., and Jimenez, J. L.: Interpretation of organic components from Positive Matrix Factorization of aerosol mass spectrometric data, Atmos. Chem. Phys., 9, 2891-2918, https://doi.org/10.5194/acp-9-2891-2009, 2009.

Updyke, K. M., Nguyen, T. B., and Nizkorodov, S. A.: Formation of brown carbon via reactions of ammonia with secondary organic aerosols from biogenic and anthropogenic precursors, Atmos. Environ., 63, 22-31, https://doi.org/10.1016/j.atmosenv.2012.09.012, 2012.

Vasilakopoulou, C. N., Florou, K., Kaltsonoudis, C., Stavroulas, I., Mihalopoulos, N., and Pandis, S. N.: Development and evaluation of an improved offline aerosol mass spectrometry technique, Atmos. Meas. Tech., 16, 2837-2850, https://doi.org/10.5194/amt-16-2837-2023, 2023.

Veld, M., Khare, P., Hao, Y. F., Reche, C., Pérez, N., Alastuey, A., Yus-Díez, J., Marchand, N., Prevot, A. S. H., Querol, X., and Daellenbach, K. R.: Characterizing the sources of ambient PM10 organic aerosol in urban and rural Catalonia, Spain, Sci. Total Environ., 902, 166440, https://doi.org/10.1016/j.scitotenv.2023.166440, 2023.

Wang, D. W., Shen, Z. X., Zhang, Q., Lei, Y. L., Zhang, T., Huang, S. S., Sun, J., Xu, H. M., and Cao, J. J.: Winter brown carbon over six of China's megacities: light absorption, molecular characterization, and improved source apportionment revealed by multilayer perceptron neural network, Atmos. Chem. Phys., 22, 14893-14904, https://doi.org/10.5194/acp-22-14893-2022, 2022a.

Wang, J. F., Ge, X. L., Sonya, C., Ye, J. H., Lei, Y. L., Chen, M. D., and Zhang, Q.: Influence of regional emission controls on the chemical composition, sources, and size distributions of submicron aerosols: Insights from the 2014 Nanjing Youth Olympic Games, Sci. Total Environ., 807, 150869, https://doi.org/10.1016/j.scitotenv.2021.150869, 2022b.

Wang, J. F., Ge, X. L., Chen, Y. F., Shen, Y. F., Zhang, Q., Sun, Y. L., Xu, J. Z., Ge, S., Yu, H.,

and Chen, M. D.: Highly time-resolved urban aerosol characteristics during springtime in Yangtze River Delta, China: insights from soot particle aerosol mass spectrometry, Atmos. Chem. Phys., 16, 9109-9127, https://doi.org/10.5194/acp-16-9109-2016, 2016.

Wang, J. F., Ye, J. H., Zhang, Q., Zhao, J., Wu, Y. Z., Li, J. Y., Liu, D. T., Li, W. J., Zhang, Y. G., Wu, C., Xie, C. H., Qin, Y. M., Lei, Y. L., Huang, X. P., Guo, J. P., Liu, P. F., Fu, P. Q., Li, Y. J., Lee, H. C., Choi, H., Zhang, J., Liao, H., Chen, M. D., Sun, Y. L., Ge, X. L., Martin, S. T., and Jacob, D. J.: Aqueous production of secondary organic aerosol from fossil-fuel emissions in winter Beijing haze, Proc. Natl. Acad. Sci. U. S. A., 118, https://doi.org/10.1073/pnas.2022179118, 2021.

Wang, K., Zhang, Y., Huang, R. J., Cao, J. J., and Hoffmann, T.: UHPLC-Orbitrap mass spectrometric characterization of organic aerosol from a central European city (Mainz, Germany) and a Chinese megacity (Beijing), Atmos. Environ., 189, 22-29, https://doi.org/10.1016/j.atmosenv.2018.06.036, 2018a.

Wang, L. W., Wang, X. F., Gu, R. R., Wang, H., Yao, L., Wen, L., Zhu, F. P., Wang, W. H., Xue, L. K., Yang, L. X., Lu, K. D., Chen, J. M., Wang, T., Zhang, Y. H., and Wang, W. X.: Observations of fine particulate nitrated phenols in four sites in northern China: concentrations, source apportionment, and secondary formation, Atmos. Chem. Phys., 18, 4349-4359, https://doi.org/10.5194/acp-18-4349-2018, 2018b.

Wang, Y., Huang, R. J., Zhong, H. B., Wang, T., Yang, L., Yuan, W., Xu, W., and An, Z. S.: Predictions of the Optical Properties of Brown Carbon Aerosol by Machine Learning with Typical Chromophores, Environ. Sci. Technol., 58, 20588-20597, https://doi.org/10.1021/acs.est.4c09031, 2024.

Wang, Y. J., Hu, M., Lin, P., Guo, Q. F., Wu, Z. J., Li, M. G., Zeng, L. M., Song, Y., Zeng, L. W., Wu, Y. S., Guo, S., Huang, X. F., and He, L. Y.: Molecular characterization of nitrogen-containing organic compounds in humic-like substances emitted from straw residue burning, Environ. Sci. Technol., 51, 5951-5961, https://doi.org/10.1021/acs.est.7b00248, 2017.

Wang, Y. Q.: An open source software suite for multi-dimensional meteorological data computation and visualisation, Journal of Open Research Software, 7, https://doi.org/10.5334/jors.267, 2019.

Wen, H., Zhou, Y., Xu, X. Y., Wang, T. S., Chen, Q. L., Chen, Q. C., Li, W. J., Wang, Z., Huang, Z. W., Zhou, T., Shi, J. S., Bi, J. R., Ji, M. X., and Wang, X.: Water-soluble brown carbon in atmospheric aerosols along the transport pathway of Asian dust: Optical properties, chemical compositions, and potential sources, Sci. Total Environ., 789, 147971, https://doi.org/10.1016/j.scitotenv.2021.147971, 2021.

Wu, G. M., Ram, K., Fu, P. Q., Wang, W., Zhang, Y. L., Liu, X. Y., Stone, E. A., Pradhan, B. B., Dangol, P. M., Panday, A. K., Wan, X., Bai, Z. P., Kang, S. C., Zhang, Q. G., and Cong, Z. Y.: Water-soluble brown carbon in atmospheric aerosols from Godavari (Nepal), a regional representative of south Asia, Environ. Sci. Technol., 53, 3471-3479, https://doi.org/10.1021/acs.est.9b00596, 2019a.

Wu, Y. Z., Ge, X. L., Wang, J. F., Shen, Y. F., Ye, Z. L., Ge, S., Wu, Y., Yu, H., and Chen, M. D.: Responses of secondary aerosols to relative humidity and photochemical activities in an industrialized environment during late winter, Atmos. Environ., 193, 66-78, https://doi.org/10.1016/j.atmosenv.2018.09.008, 2018.

Wu, Y. Z., Liu, D. T., Wang, J. F., Shen, F. Z., Chen, Y. F., Cui, S. J., Ge, S., Wu, Y., Chen, M. D., and Ge, X. L.: Characterization of size-resolved hygroscopicity of black carbon-containing

particle in urban environment, Environ. Sci. Technol., 53, 14212-14221, https://doi.org/10.1021/acs.est.9b05546, 2019b.

Xian, J. K., Cui, S. J., Chen, X. Z., Wang, J. Y., Xiong, Y. F., Gu, C. J., Wang, Y., Zhang, Y. J., Li, H. W., Wang, J. F., and Ge, X. L.: Online chemical characterization of atmospheric fine secondary aerosols and organic nitrates in summer Nanjing, China, Atmos. Res., 290, 106783, https://doi.org/10.1016/j.atmosres.2023.106783, 2023.

Xie, M. J., Mladenov, N., Williams, M. W., Neff, J. C., Wasswa, J., and Hannigan, M. P.: Water soluble organic aerosols in the Colorado Rocky Mountains, USA: composition, sources and optical properties, Sci. Rep., 6, 39339, https://doi.org/10.1038/srep39339, 2016.

Xie, X. C., Chen, Y. F., Nie, D. Y., Liu, Y., Liu, Y., Lei, R. Y., Zhao, X. Y., Li, H. W., and Ge, X. L.: Light-absorbing and fluorescent properties of atmospheric brown carbon: A case study in Nanjing, China, Chemosphere, 251, 126350, https://doi.org/10.1016/j.chemosphere.2020.126350, 2020.

Xing, C., Wan, Y. B., Wang, Q. Q., Kong, S. F., Huang, X. P., Ge, X. L., Xie, M. J., and Yu, H.: Molecular Characterization of Brown Carbon Chromophores in Atmospherically Relevant Samples and Their Gas-Particle Distribution and Diurnal Variation in the Atmosphere, J. Geophys. Res.: Atmos., 128, e2022JD038142, https://doi.org/10.1029/2022JD038142, 2023.

Xu, L. L., Lin, G. X., Liu, X. H., Wu, C. L., Wu, Y. F., and Lou, S. J.: Constraining Light Absorption of Brown Carbon in China and Implications for Aerosol Direct Radiative Effect, Geophys. Res. Lett., 51, https://doi.org/10.1029/2024gl109861, 2024.

Yan, G. and Kim, G.: Speciation and sources of brown carbon in precipitation at seoul, Korea: insights from excitation–emission matrix spectroscopy and carbon isotopic analysis, Environ. Sci. Technol., 51, 11580-11587, https://doi.org/10.1021/acs.est.7b02892, 2017.

Yan, J. P., Wang, X. P., Gong, P., Wang, C. F., and Cong, Z. Y.: Review of brown carbon aerosols: recent progress and perspectives, Sci. Total Environ., 634, 1475-1485, https://doi.org/10.1016/j.scitotenv.2018.04.083, 2018.

Yassine, M. M., Harir, M., Dabek-Z., E., and Schmitt-K., P.: Structural characterization of organic aerosol using Fourier transform ion cyclotron resonance mass spectrometry: Aromaticity equivalent approach, Rapid Commun. Mass Spectrom., 28, 2445-2454, https://doi.org/doi.org/10.1002/rcm.7038, 2014.

Ye, Z. L., Qu, Z. X., Ma, S. S., Luo, S. P., Chen, Y. T., Chen, H., Chen, Y. F., Zhao, Z. Z., Chen, M. D., and Ge, X. L.: A comprehensive investigation of aqueous-phase photochemical oxidation of 4-ethylphenol, Sci. Total Environ., 685, 976-985, https://doi.org/10.1016/j.scitotenv.2019.06.276, 2019.

Ye, Z. L., Li, Q., Liu, J. S., Luo, S. P., Zhou, Q. F., Bi, C. L., Ma, S. S., Chen, Y. F., Chen, H., Li, L., and Ge, X. L.: Investigation of submicron aerosol characteristics in Changzhou, China: Composition, source, and comparison with co-collected PM2.5, Chemosphere, 183, 176-185, https://doi.org/10.1016/j.chemosphere.2017.05.094, 2017.

Yu, H. R., Liang, H., Qu, F. S., Han, Z. S., Shao, S. L., Chang, H. Q., and Li, G. B.: Impact of dataset diversity on accuracy and sensitivity of parallel factor analysis model of dissolved organic matter fluorescence excitation-emission matrix, Sci. Rep., 5, 10207, https://doi.org/10.1038/srep10207, 2015.

Yu, J. T., Yan, C. Q., Liu, Y., Li, X. Y., Zhou, T., and Zheng, M.: Potassium: a tracer for biomass burning in Beijing?, Aerosol Air Qual. Res., 18, 2447-2459,

https://doi.org/10.4209/aaqr.2017.11.0536, 2018.

Zhang, B. Q., Zhang, Y. J., Zhang, K. X., Zhang, Y. C., Ji, Y., Zhu, B. Z., Liang, Z. Y., Wang, H. L., and Ge, X. L.: Machine learning assesses drivers of PM2.5 air pollution trend in the Tibetan Plateau from 2015 to 2022, Sci. Total Environ., 878, 163189, https://doi.org/10.1016/j.scitotenv.2023.163189, 2023.

Zhang, Q., Jimenez, J. L., Canagaratna, M. R., Ulbrich, I. M., Ng, N. L., Worsnop, D. s. R., and Sun, Y. L.: Understanding atmospheric organic aerosols via factor analysis of aerosol mass spectrometry: a review, Anal. Bioanal. Chem., 401, 3045-3067, https://doi.org/10.1007/s00216-011-5355-y, 2011.

Zhang, S. Y.: Detection of scopolamine in nori fruit juice and its traditional chinese medicine compound health products by high performance liquid chromatography, World Latest Medicine Information, 18, 91-92, https://doi.org/10.19613/j.cnki.1671-3141.2018.82.066, 2018.

Zhang, X. L., Lin, Y. H., Surratt, J. D., and Weber, R. J.: Sources, composition and absorption Ångström exponent of light-absorbing organic components in aerosol extracts from the Los Angeles basin, Environ. Sci. Technol., 47, 3685-3693, https://doi.org/10.1021/es305047b, 2013.

Zhang, Y. Z., Forrister, H., Liu, J. M., Dibb, J., Anderson, B., Schwarz, J. P., Perring, A. E., Jimenez, J. L., Campuzano-Jost, P., Wang, Y. H., Nenes, A., and Weber, R. J.: Top-of-atmosphere radiative forcing affected by brown carbon in the upper troposphere, Nat. Geosci., 10, 486-489, https://doi.org/10.1038/ngeo2960, 2017.

Zhao, R., Lee, A. K. Y., Huang, L., Li, X., Yang, F., and Abbatt, J. P. D.: Photochemical processing of aqueous atmospheric brown carbon, Atmos. Chem. Phys., 15, 6087-6100, https://doi.org/10.5194/acp-15-6087-2015, 2015.

Zhong, M., Xu, J. Z., Wang, H. Q., Gao, L., Zhu, H. X., Zhai, L. X., Zhang, X. H., and Zhao, W. H.: Characterizing water-soluble brown carbon in fine particles in four typical cities in northwestern China during wintertime: integrating optical properties with chemical processes, Atmos. Chem. Phys., 23, 12609-12630, https://doi.org/10.5194/acp-23-12609-2023, 2023.

Zhu, B., Fang, J., Zhang, Y., Qiu, J., Chen, K., Zhang, K., Liang, H., Yang, H., Ding, Y., and Ge, X.: Machine learning elucidates ubiquity of enhanced ozone air pollution in China linked to the spring festival effect, Atmos. Pollut. Res., 15, 102127, https://doi.org/10.1016/j.apr.2024.102127, 2024.

Zorn, S. R., Drewnick, F., Schott, M., Hoffmann, T., and Borrmann, S.: Characterization of the South Atlantic marine boundary layer aerosol using an aerodyne aerosol mass spectrometer, Atmos. Chem. Phys., 8, 4711-4728, https://doi.org/10.5194/acp-8-4711-2008, 2008.

Zsolnay, A., Baigar, E., Jimenez, M., Steinweg, B., and Saccomandi, F.: Differentiating with fluorescence spectroscopy the sources of dissolved organic matter in soils subjected to drying, Chemosphere, 38, 45-50, https://doi.org/10.1016/S0045-6535(98)00166-0, 1999.

1480   Table 1. The average mass concentrations of major chemical components as well as the

1481   parameters of optical properties of $PM_{2.5}$ collected in Nanjing during two seasons.

	Summer Season (SS)			Cold Season (CS)		
	Daytime	Nighttime	Average	Daytime	Nighttime	Average
OC ($\mu g\ m^{-3}$)	7.02±3.04	6.87±2.51	6.94±2.76	12.9±5.77	12.74±5.29	12.82±5.51
EC ($\mu g\ m^{-3}$)	1.13±0.31	1.22±0.37	1.17±0.34	1.94±0.93	1.6±0.74	1.77±0.86
AAE_{WSOC}	6.34±0.65	6.35±0.69	6.35±0.67	6.43±0.68	6.44±0.86	6.43±0.77
AAE_{MSOC}	6.02±0.90	5.96±0.96	5.99±0.92	7.06±0.94	6.70±0.65	6.89±0.82
WSOC ($\mu g\ m^{-3}$)	4.06±1.31	4.45±1.44	4.26±1.38	5.81±2.29	5.75±2.25	6.34±2.27
MSOC ($\mu g\ m^{-3}$)	5.64±2.12	5.79±1.89	5.72±1.99	10.42±4.98	10.49±4.57	10.45±4.75
Total ions ($\mu g\ m^{-3}$)	18.00±5.49	18.69±8.05	18.49±6.91	35.41±15.02	43.12±17.94	39.22±16.88
$Abs_{365,\ WSOC}$ (M m^{-1})	2.15±0.90	2.38±0.80	2.27±0.85	4.89±2.63	4.86±2.46	4.87±2.53
$Abs_{365,\ MSOC}$ (M m^{-1})	3.44±1.40	3.82±1.55	3.64±1.48	4.65±2.24	5.31±2.71	4.97±2.49
$MAE_{365,\ WSOC}$ ($m^2\ g^{-1}$)	0.54±0.16	0.56±0.15	0.55±0.16	0.73±0.20	0.77±0.21	0.75±0.21
$MAE_{365,\ MSOC}$ ($m^2\ g^{-1}$)	0.68±0.32	0.75±0.30	0.72±0.31	0.48±0.18	0.52±0.16	0.50±0.17
SFE_{WSOC} (W g^{-1})	2.16±1.29	2.24±1.36	2.20±1.33	3.16±1.8	3.42±1.25	3.24±1.84
SFE_{MSOC} (W g^{-1})	2.28±2.37	2.55±1.85	2.43±2.10	2.19±1.01	2.26±0.81	2.23±0.91

1482

1483   Table 2. Multi-linear regression results of the four factors and corresponding average

1484   contributions to the total light absorption of water-soluble organics (WSOA).

Factor	Regression Coefficient($m^2 \cdot g^{-1}$)		Contribution (%)
	Average	Standard Error	
HOA	0.71	0.11	33.05
BBOA	0.71	0.06	15.49
OOA1	0.12	0.07	6.00
OOA2	0.83	0.14	45.46

1485

1486   Table 3. The average values of fluorescence indices of both water-soluble organic

1487   carbon (WSOC) and methanol-soluble organic carbon (MSOC).

	Summer Season (SS)			Cold Season (CS)		
	Day	Night	Average	Day	Night	Average
HIX_{WSOC}	3.16±0.74	3.51±1.12	3.34±0.97	4.68±0.94	4.67±0.91	4.68±0.92
HIX_{MSOC}	2.65±0.99	2.78±0.86	2.72±0.92	3.42±0.73	3.53±0.58	3.48±0.66
FI_{WSOC}	1.85±0.16	1.97±0.17	1.91±0.18	1.89±0.11	1.92±0.09	1.90±0.10
FI_{MSOC}	2.25±0.26	2.30±0.31	2.27±0.28	2.10±0.15	2.12±0.14	2.11±0.15
BIX_{WSOC}	0.81±0.16	0.86±0.14	0.84±0.15	0.86±0.10	0.91±0.08	0.88±0.09
BIX_{MSOC}	0.89±0.19	0.9±0.13	0.90±0.16	0.95±0.10	0.97±0.11	0.96±0.10

1488

1489   Table 4. The number percentages of organosulfates (OSs) in CHOS compounds in ESI$^-$

1490   mode and those of nitrooxy-OSs in CHONS compounds in both modes.

	SS		CS	
	Daytime	Nighttime	Daytime	Nighttime
OSs (ESI$^-$)	34.8%	42.3%	54.3%	68.6%
Nitrooxy-OSs (ESI$^-$)	5.3%	12.0%	11.0%	12.5%
Nitrooxy-OSs (ESI$^+$)	10.3%	11.8%	10.5%	9.8%

1491

1492
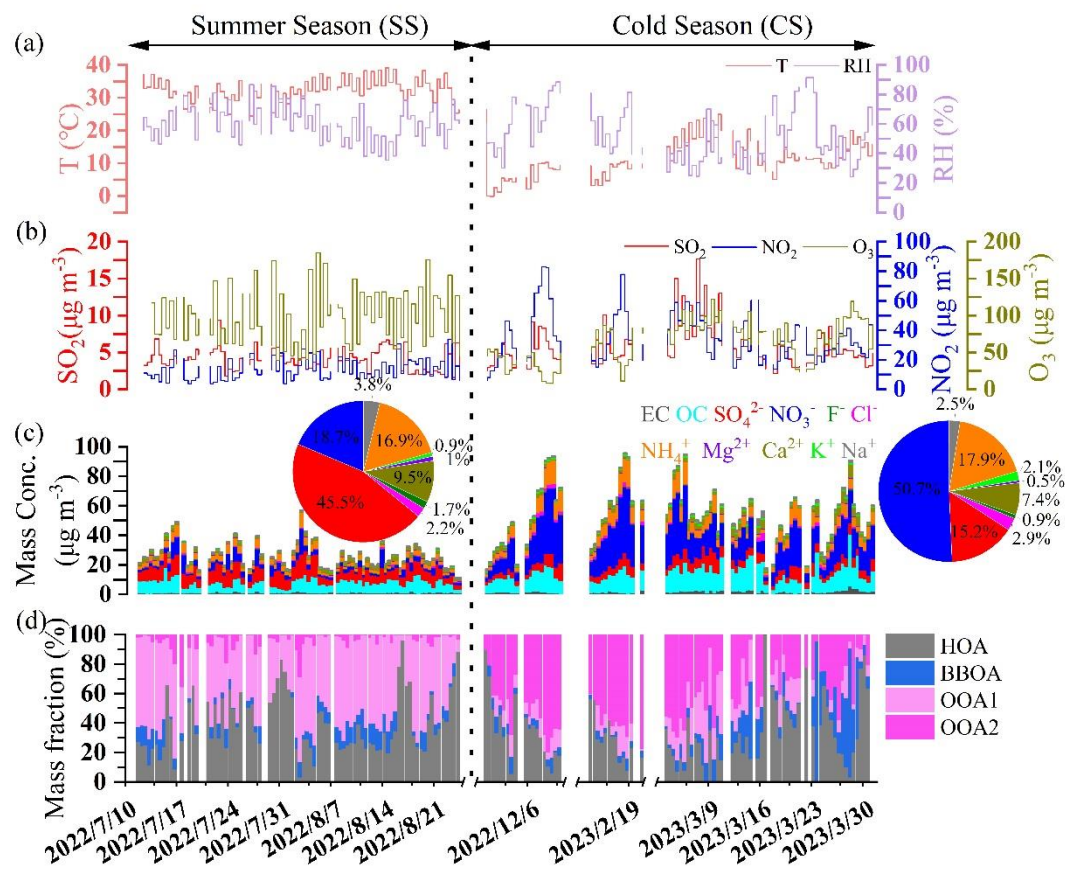
1493

1494 Figure 1. Time series of: (a) air temperature (T) and relative humidity (RH); (b)

1495 concentrations of nitrogen dioxide (NO_2), sulfur dioxide (SO_2) and ozone (O_3); (c)

1496 concentrations of different inorganic ions, total organic carbon (OC), and elemental

1497 carbon (EC) (two inset pies are the average mass contributions of difference ions to the

1498 total ions during SS and CS, respectively); and (d) mass percentages of different factors

1499 with respect to the total water-soluble OA

1500
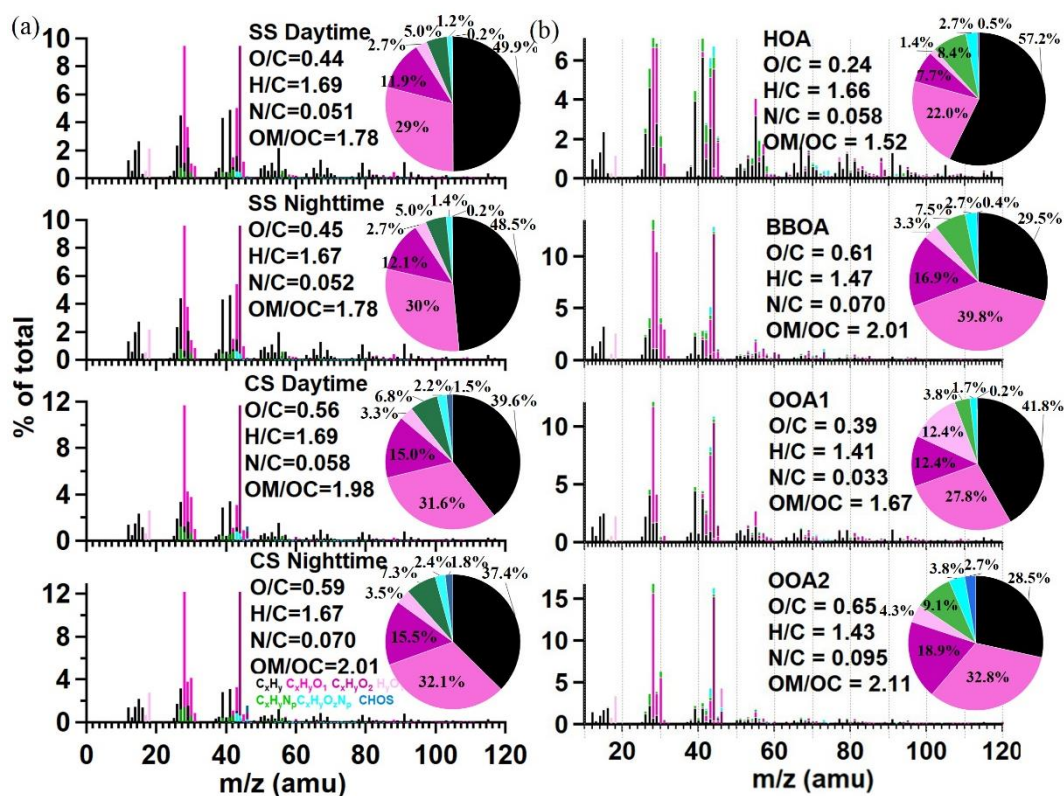
1501

1502 Figure 2. High-resolution mass spectra (HRMS) of (a) the water-soluble OA (WSOA)

1503 during different periods, and (b) the four resolved factors (HOA, BBOA, OOA1,

1504 OOA2). Ions are classified into and colored by different ion families, and inset pies in

1505 both charts show the mass fractional contributions of different ion families to the total

1506 HRMS correspondingly.

1507

1508
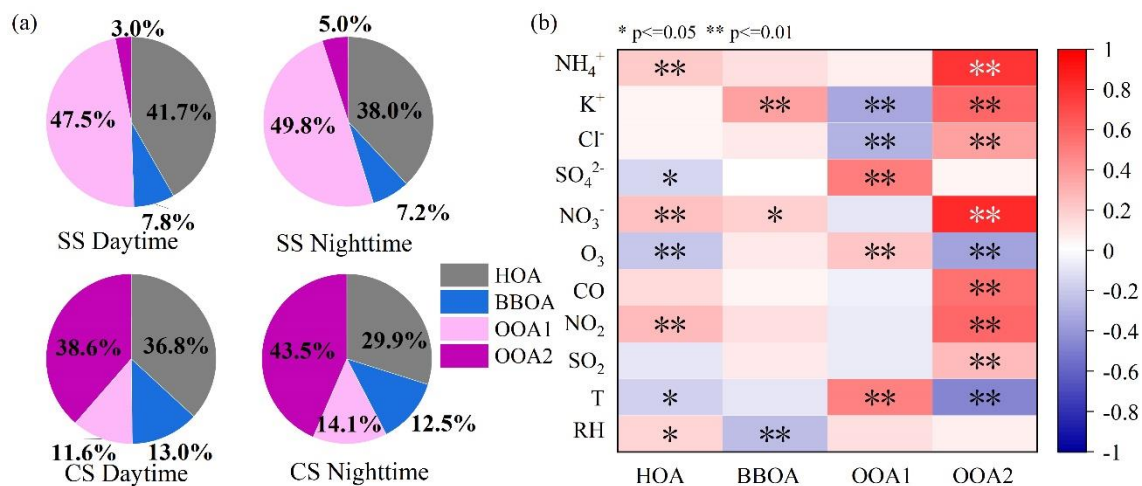
1509 Figure 3. (a) Average mass contributions of the four factor to WSOA during different

1510 periods, and (b) cross-correlation coefficients (Pearson's *r*) among the four factors and

1511 other aerosol components as well as gaseous species.

1512

1513
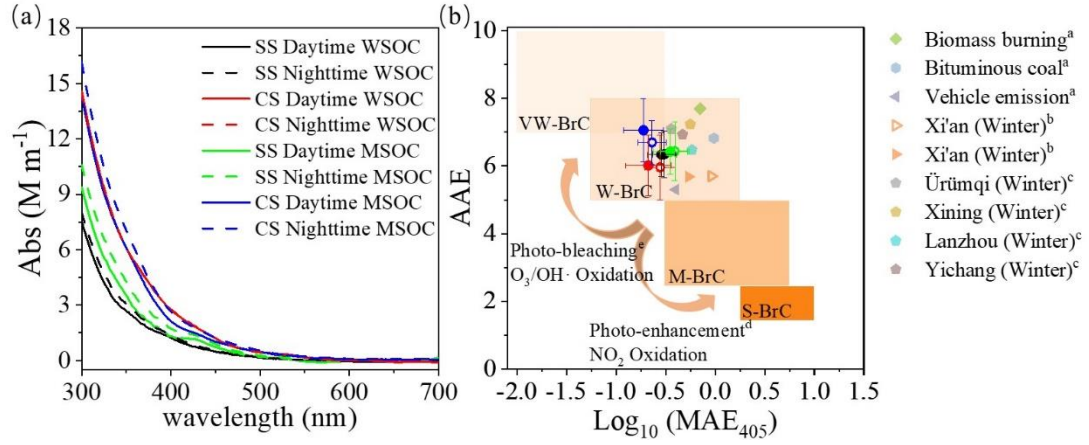
1514 Figure 4. (a) Light absorption coefficients (Abs) of the water-soluble OC (WSOC) and

1515 methanol-soluble OC (MSOC) as a function of wavelength, and (b) distribution of the

1516 measured data in the $\log_{10}(MAE_{405})$-AAE space (Saleh, 2020)(MAE_{405}: Mass

1517 absorption efficiency at 405 nm; AAE: Absorption Ångström Exponent; The shaded

1518 areas indicate very weakly (VW), weakly (W), moderately (M), and strongly (S)

1519 absorbing brown carbon (BrC), respectively; Other markers indicate results from [a]

1520 Huang et al. (2018), [b] Chen et al. (2018) and [c] Zhong et al. (2023).

1521

1522
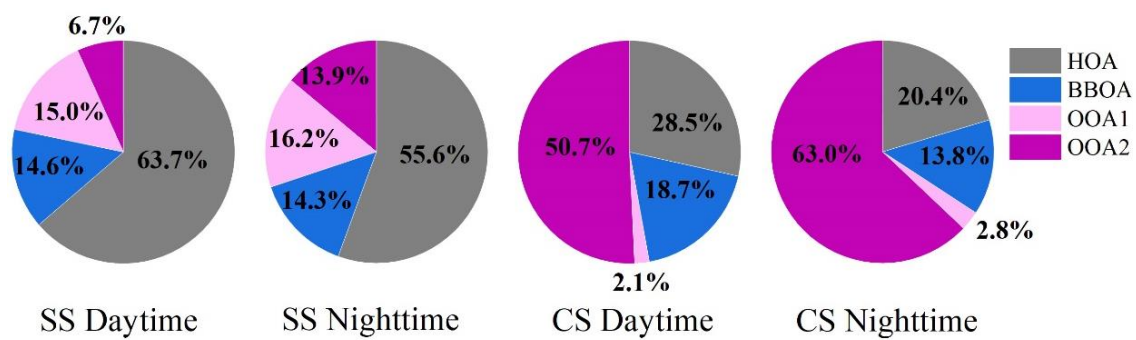
1523   Figure 5. Contributions of the four factors to the total light absorption of WSOA during

1524   different periods.

1525

1526 Figure 6. Scatter plot of MAE$_{365}$ (mass absorption efficiency at 365 nm) versus the

1527 oxygen-to-carbon (O/C) ratios for the WSOA.
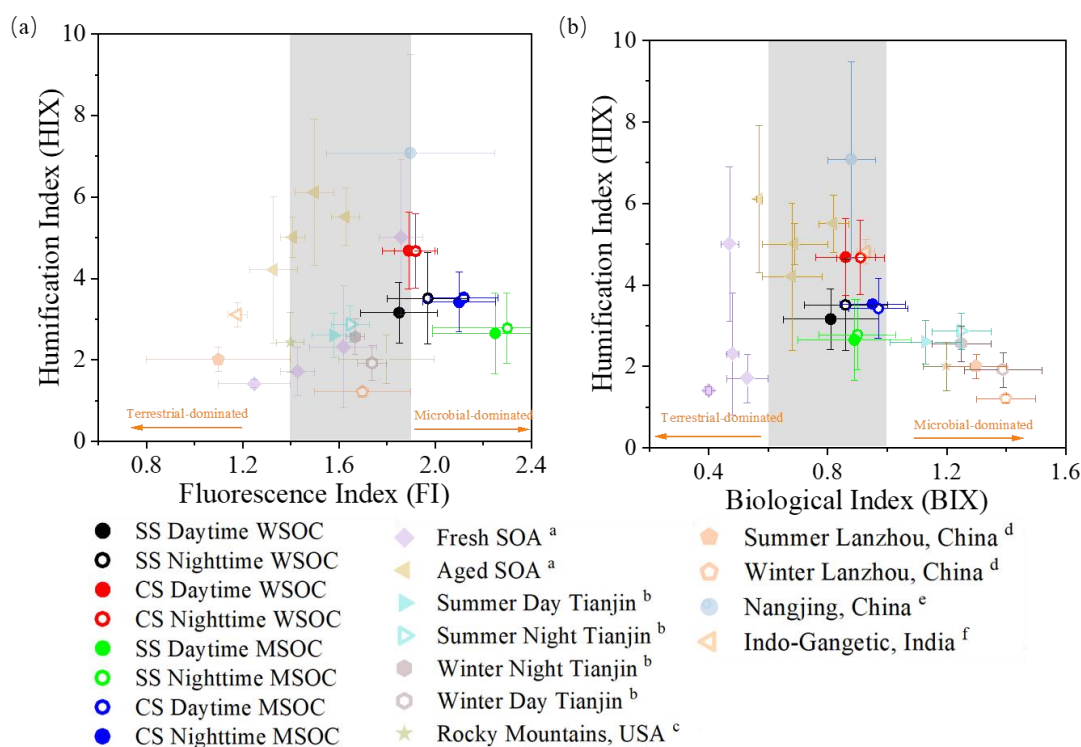
Figure 7. Distribution of the fluorescent indices of measured data in this study and a few other studies ([a] Lee et al. (2013), [b] Deng et al. (2022), [c] Xie et al. (2016), [d] Qin et al. (2018), [e] Xie et al. (2016), [f] Dey et al. (2021)): (a) Humidication index (HIX) versus fluorescenc index (FI), and (b) HIX versus biological index (BIX). The shaded areas marked 0.6 ~ 1 of BIX (Huguet et al., 2009) and 1.6 ~ 1.9 of FI (Mcknight et al., 2001).

1535

1536
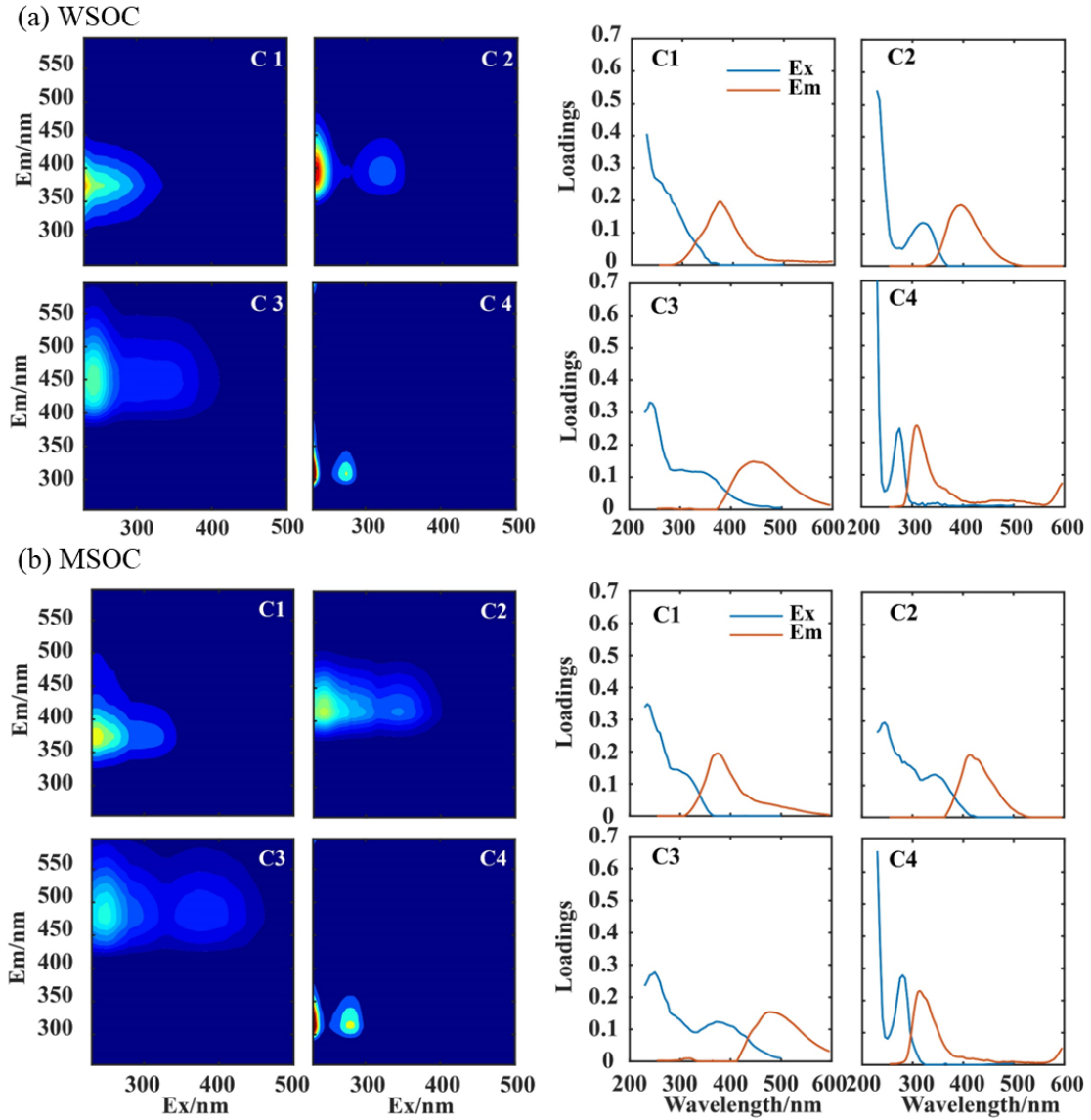
Figure 8. Four fluorescence components (C1 ~ C4) and the corresponding fluorescent

intensities of emission (brown) and excitation (blue) against wavelenghth: (a) WSOC,

and (b) MSOC.

1540

1541

1542
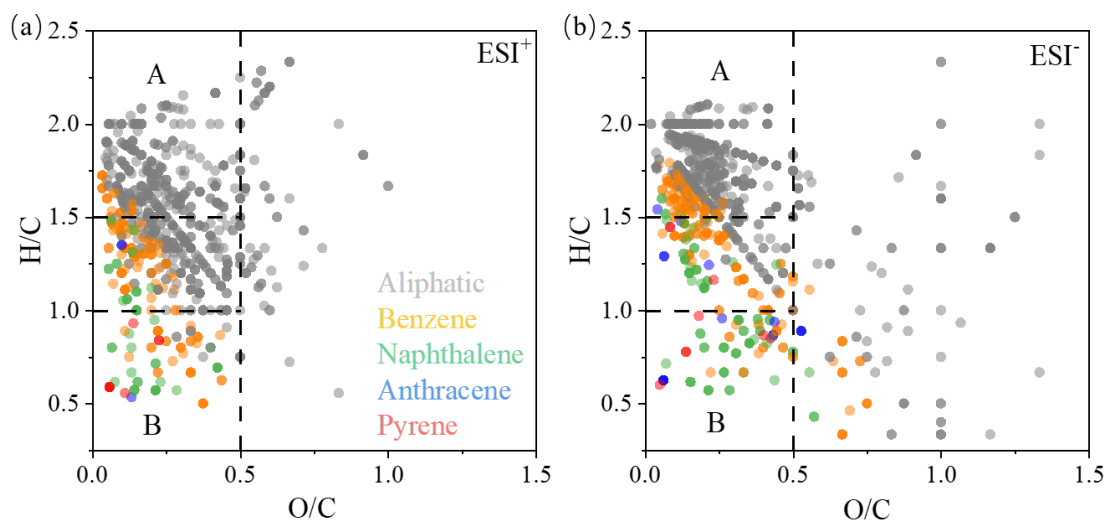
1543 Figure 9. Van Krevelen diagram for CHO compounds detected in (a) ESI[+] and (b) ESI[-]

1544 mode. The markers with different colors represent aliphatic compounds (Xc < 2.50),

1545 aromatic benzene ring structures (2.50 ≤ Xc <2.71), naphthalene ring structures (2.71

1546 ≤ Xc <2.80), anthracene ring structures (2.80 ≤ Xc <2.83), and pyrene ring structures

1547 (2.83 ≤ Xc <2 .92), respectively (Mao et al., 2022).

1548

1549
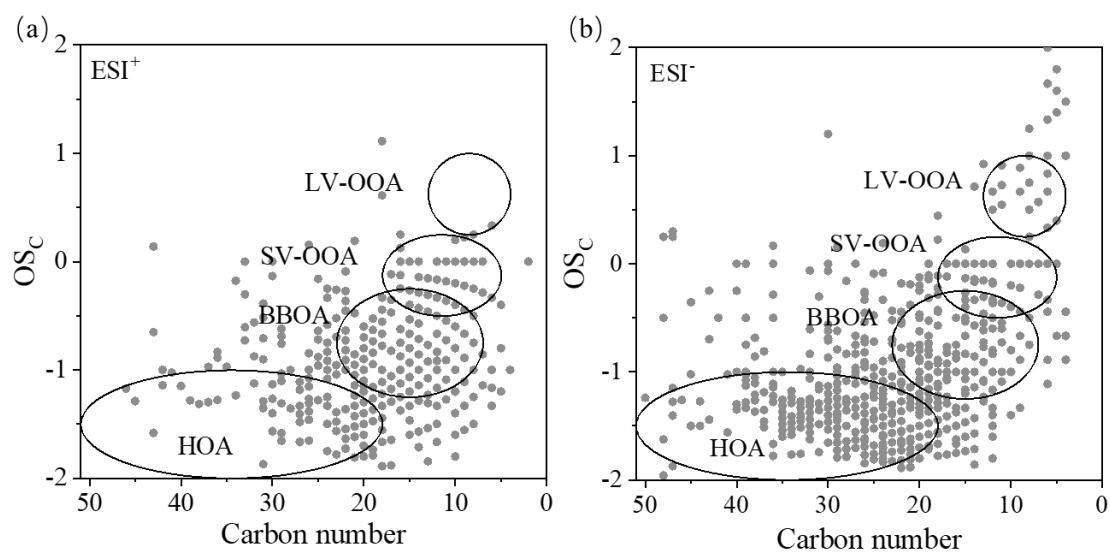
1550 Figure 10. Scatter plots of carbon oxidation state (OSc) versus carbon number for CHO

1551 compounds: (a) ESI⁺ mode, and (b) ESI⁻ mode. The circled areas represent those from

1552 fossil fuel combustion hydrocarbon-like OA (HOA), biomass burning OA (BBOA),

1553 semi-volatile oxygenated OA (SV-OOA) and low-volatility oxygenated OA (LV-

1554 OOA)(Kroll et al., 2011).

1555

1-$C_6H_{15}NO(CH_2)_n$ 2-$C_6H_{15}NO_2(CH_2)_n$ 3-$C_4H_9NO(CH_2)_n$

4-$C_4H_9NO_2(CH_2)_n$ 5-$C_3H_5NO(CH_2)_n$ 6-$C_6H_8N_2O_2(CH_2)_n$

7-$C_9H_6NO(CH_2)_n$ 8-$C_5H_6N_2O(CH_2)_n$ 9-$C_5H_5NO(CH_2)_n$

10-$C_7H_7NO(CH_2)_n$ 11-$C_8H_7NO(CH_2)_n$ 12-$C_9H_7NO(CH_2)_n$

1-$C_6H_4N_2O_5(CH_2)_n$ 2-$C_6H_5NO_4(CH_2)_n$ 3-$C_8H_7NO_4(CH_2)_n$

4-$C_6H_5NO_3(CH_2)_n$ 5-$C_8H_7NO_3(CH_2)_n$ 6-$C_{10}H_7NO_3(CH_2)_n$
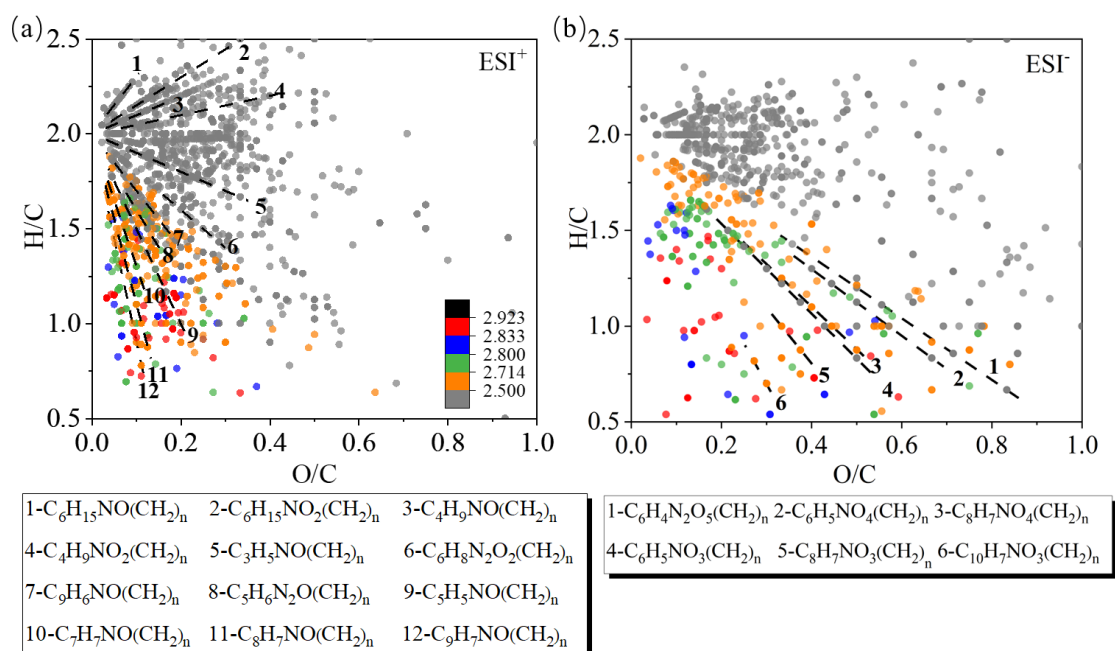
Figure 11. Van Krevelen diagram for CHON compounds detected in both ESI$^+$ and ESI$^-$

mode. The data are also colored by Xc values (See caption of Fig. 9), and the different

dash lines represent different series of compounds.

1562
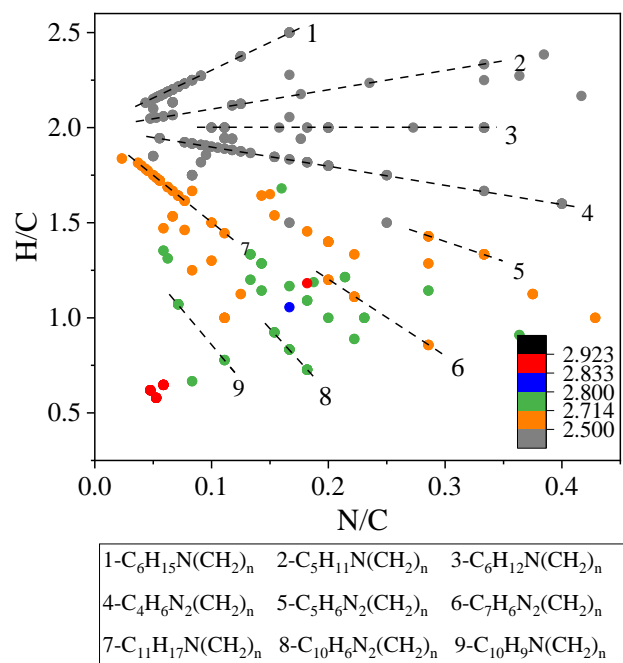
1563

1564

1565 Figure 12. Van Krevelen diagram of the CHN compounds in ESI$^+$ mode. The data are

1566 also colored by Xc values (See caption of Fig. 9), and the different dash lines represent

1567 different series of compounds.

1568

1569
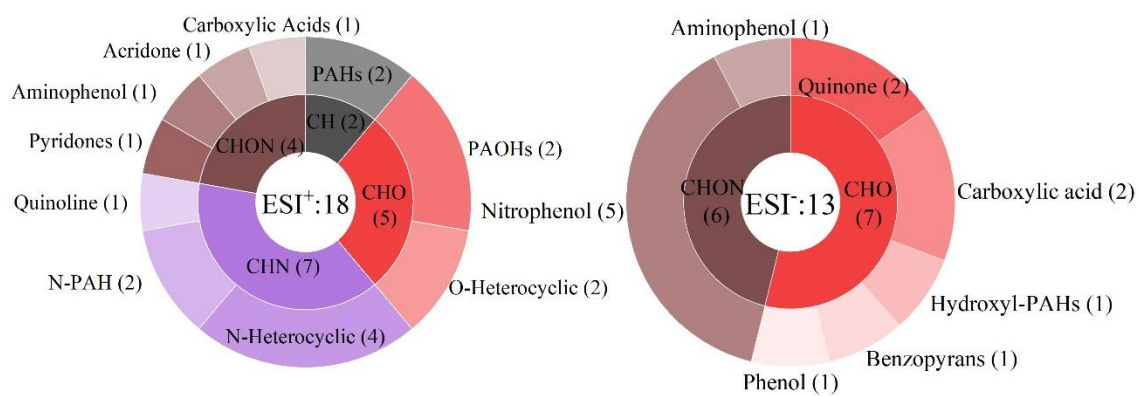
1570   Figure 13. Distributions of the machine learning identified key light absorbing organic

1571   compounds (details in Table S2 in the supplement)

1572